Anodized titanium oxide thickness estimation with ellipsometry, reflectance spectra extrema positions and electronic imaging: importance of the interfaces electromagnetic phase-shift

Quentin Cridling, Renée Charrière, D. Jamon, Matthieu Lenci, Mariapia Pedeferri, David Delafosse Delafosse

Anodized titanium oxide thickness estimation with ellipsometry, reflectance spectra extrema positions and electronic imaging: importance of the interfaces electromagnetic phase-shift

CRIDLING Quentin[1,2]*, CHARRIERE Renee[1], JAMON Damien[3], LENCI Matthieu[1], PEDEFERRI MariaPia[2], DELAFOSSE David[1,2] ; [1]Mines Saint-Etienne, Univ Lyon, CNRS, UMR 5307 LGF, Centre SMS, F - 42023 Saint-Etienne France; [2]Politecnico di Milano, Department of Chemistry, Materials and Chemical Engineering "Giulio Natta", Milan, Italy; [3]Laboratoire Hubert Curien CNRS, UMR5516, Université de Lyon, Université de Saint-Etienne, Jean Monnet, F-42000, Saint-Etienne, France

corresponding author: Q.cridling@gmail.com

Abstract

The oxide thickness of anodized titanium samples has been determined through ellipsometry, reflectance spectra extrema positions and electronic imaging. The reflectance spectra extrema position technique is applicable in the case were the oxide layer is thin enough to generate an interference phenomenon inside the oxide layer. When reflected at the air/oxide and oxide/metal interfaces, the electromagnetic field undergoes a phase-shift, which is often neglected in the literature. By comparing the oxide thickness obtained through the different techniques, it is shown that this phase-shift isn't negligible for thin oxide layers. The relative error on the oxide thickness is for example of about 50% for a 17 nm thick oxide layer. By studying the discrepancy observed in the literature for the titanium and oxide layer refractive indexes, which is of about 13% in the wavelength range [350 nm – 600 nm], the error induced when neglecting the electromagnetic phase-shift is higher than the error induced by the uncertainty on the refractive indexes for oxide thicknesses below about 50 nm.

Keywords: titanium anodizing, oxide thickness determination, interference phenomenon, ellipsometry, Focused Ion Beam lamellae, reflectance spectrum, electromagnetic phase-shift

1. Introduction

Oxidized titanium, that is titanium on which the natural oxide layer has been grown artificially, can exhibit photocatalytic properties [1,2]. It is also highly resistive to corrosion [3,4] and biocompatible [5–7]. Under certain conditions, oxidized titanium may have an interferential coloration [8]. Both its biocompatibility and coloration properties make oxidized titanium a promising material to improve the esthetic rendering of dental implants abutments [9] or prosthetic cornea backplates [10], for the creation of jewels with innovative designs [11]. Oxidized titanium is also used for artistic paintings [12].

Titanium oxidation can be forced through various techniques such as heating [13], pulsed [14,15] or continuous [16] laser irradiation, anodizing [1,4–6,8,9,17,18], micro-arc oxidation (also called plasma electrolytic oxidation or anodic spark deposition) [3,7,19,20] or even mixed methods [21]. The present paper will focus on anodizing, as it is the best-suited method to generate uniform oxide films with homogeneous interferential colors.

The oxide thickness can be characterized through numerous techniques [8,16,22–31]. Anodized titanium oxide thickness generally lies in the range [10 nm – 300 nm] and the oxide layer is homogeneous enough to generate reflectance spectra which shape (in or close to the visible wavelengths range) is dominated by the interference phenomenon occurring inside the thin oxide layer. Thus, the reflectance spectrum local extrema positions can be linked to the oxide layer thickness. Note that this method implies to know the oxide (and in some cases the substrate) refractive index. Even though this method is widely used for oxide thickness determination, very few papers take into account the electromagnetic phase-shift which occurs at the reflection on the air/oxide and oxide/metal interfaces when establishing the formula linking the positions of the extrema to the oxide thickness. Bartlett [27] , Di Quarto et al. [32], Sharma et al. [33], Karambakhsh

et al. [34], Manjaiah et al. [35], Balaji et al. [36], Van Gils et al. [37], Ling Yang et al. [38] and Diamanti et al. [39] neglect this phase-shift, whereas Fuhrman et al. [40] mention it but don't give a detailed calculation of its theoretical value. Charlesby et al. [41] characterized anodized tantalum samples by taking into account the electromagnetic phase-shift. They developed an original method to determine experimentally at the same time the variations of the oxide refractive index with the wavelength, the oxide layer thickness, and the evolution with wavelength of the oxide/metal electromagnetic phase-shift. Winterbottom [42] gave theoretical relationships between the reflectance spectra extrema positions and the oxide layer thickness taking into account the oxide/metal electromagnetic phase-shift. He also compared oxide thickness values estimated with and without taking into account the oxide/metal electromagnetic phase-shift for various oxide/metal systems (Cu_2O/Cu, Fe_2O_3/Fe, Al_2O_3/Al) and showed that the thickness estimation error can reach about 200% when the phase-shift is neglected. Pliskin [43] established theoretical formulas of the electromagnetic phase-shift for Transverse Electric (TE) and Transverse Magnetic (TM) electric field polarizations and computed phase-shift thickness correction charts for various systems as for example silicon dioxide (SiO_2)/Aluminum, SiO_2/Chromium, Alumina/Germanium, etc… with the refractive indexes of the different materials extracted from the literature.

Some papers concluded of a good agreement between oxide thickness determination from reflectance spectra extrema without taking into account the phase-shift and other techniques such as ellipsometry [8,37], Auger electron spectroscopy [38] or Transmission electron microscopy (TEM) images of sample lamellae cut out with a Focused ion beam (FIB) [27]. Nevertheless, Diamanti et al. [8] and Van Gils et al. [37] didn't take the same oxide layer refractive index for the reflectance extrema oxide thickness determination as this obtained through ellipsometry. Ling Yang et al. [38] took an average value extracted from the literature of 2.4 for the oxide layer refractive index, and Bartlett [27] took different values of the oxide layer refractive index of either 2.33 or 2.37 when performing the thickness comparisons with the TEM images. In the present paper, the oxide

thickness values obtained from the reflectance spectra extrema have been compared with thicknesses obtained with ellipsometric measurements. To ensure a correct estimation of the error on the oxide thickness determination when neglecting the electromagnetic phase-shift, the refractive index values used for the reflectance extrema oxide thickness determinations correspond to the refractive index values measured through ellipsometry on the same samples. Also, as oxide thicknesses determined from reflectance extrema and ellipsometry are based on the same refractive indexes, direct electronic imaging of foils cut out with a FIB has been performed to validate the oxide thickness estimations. By studying the discrepancy observed in the literature for the refractive indexes of titanium and anodically grown (in conditions similar to these of the present study) titanium oxide layers, the error induced on the oxide thickness when neglecting the electromagnetic phase-shift is compared to the error induced by the uncertainty on the refractive indexes.

The paper is organized as following. It first recalls the formulas giving the oxide thickness from reflectance maxima and minima positions for non-polarized light with and without taking into account the electromagnetic phase-shift. After a presentation of the experimental conditions, the results are exposed. The oxide thickness values obtained from the ellipsometric measurements, the electronic images of FIB lamellae and the reflectance spectra extrema with and without considering the interfaces electromagnetic phase-shift are presented. The last part of the paper is dedicated to discussions of the results.

2. Theory: computing oxide thickness from reflectance spectra extrema positions

In this section, we will recall the formulas giving the oxide thickness from the reflectance spectra extrema positions in the case of non-polarized light**.** The formulas will be given in two different cases: when the electromagnetic phase-shift which occurs at the reflection on the air/oxide and oxide/metal interfaces is taken into account and when this phase-shift is neglected. The theory establishing these formulas is described in details in [44]. The material is considered here as a

homogeneous semi-infinite titanium (Ti) substrate with a refractive index n_{Ti} covered by a homogeneous titanium dioxide (TiO_2) layer of refractive index n_{TiO_2} (see Figure 1). A light ray is incident on the material with an incidence angle θ_i. This ray is then split into two parts: one is reflected at the Air/TiO_2 interface and the other one is refracted inside the TiO_2 layer with an angle θ_r given by the relationship

$$\cos(\theta_r) = \sqrt{1 - \left(\frac{\sin(\theta_i)}{n_{TiO_2}}\right)^2}$$

The interference between these two rays is the origin of the extrema of the reflectance spectra.

Figure 1: Model material considered for the estimation of the oxide layer thickness $\boldsymbol{e}$ from the reflectance spectra extrema: a homogeneous semi-infinite titanium (Ti) substrate with a refractive index $\boldsymbol{n_{Ti}}$ covered by a homogeneous titanium dioxide (TiO_2) layer of refractive index $\boldsymbol{n_{TiO_2}}$. A light ray is incident on the material with an incidence angle $\boldsymbol{\theta_i}$. This ray is then split into two parts: one is reflected at the Air/TiO_2 interface and the other one is refracted inside the TiO_2 layer with an angle $\boldsymbol{\theta_r}$. $\boldsymbol{\Phi^P_{TiO_2}}$ and $\boldsymbol{\Phi^P_{Ti}}$ are the phase-shifts undergone by the electric field of polarization $\boldsymbol{P = TE}$ or $\boldsymbol{TM}$ respectively at the Air/TiO_2 interface and at TiO_2/Ti interface.

When the interfaces phase-shift is taken into account, the formulas giving the oxide thickness e from the reflectance spectra minima and maxima positions are the followings, in the case of non-polarized light:

$$\begin{cases} \text{for a wavelength position } \lambda_{max} \text{ of a maximum:} \\ e = \dfrac{\lambda_{max}}{4\pi n_{TiO_2}\cos(\theta_r)} \times [-\Phi + 2m\pi] \quad m \in \mathbb{N}^* \\ \text{for a wavelength position } \lambda_{min} \text{ of a minimum:} \\ e = \dfrac{\lambda_{min}}{4\pi n_{TiO_2}\cos(\theta_r)} \times [-\Phi + (2m+1)\pi] \quad m \in \mathbb{N} \end{cases}, \tag{1}$$

where $\boldsymbol{\Phi}$ is the average phase-shift at the reflection on the Air/TiO_2 and TiO_2/Ti interfaces for non-polarized light. These formulas assume that the oxide layer isn't absorbent, that is that $\boldsymbol{n_{TiO_2}}$ doesn't have an imaginary part. $\boldsymbol{m}$ is the interference order. $\boldsymbol{\Phi}$ is given by the relationship:

$$\Phi = \frac{1}{2}\left(\Phi^{TE}_{Ti} - \Phi^{TE}_{TiO_2}\right)[2\pi] + \frac{1}{2}\left(\Phi^{TM}_{Ti} - \Phi^{TM}_{TiO_2}\right)[2\pi], \tag{2}$$

with $\Phi^{\mathrm{P}}_{TiO_2}$ and Φ^{P}_{Ti} the phase-shifts undergone by the electric field of polarization $P = TE$ or TM when reflected respectively at the Air/TiO_2 interface and at the TiO_2/Ti interface. These quantities are defined as:

$$\begin{cases} \Phi^{P}_{TiO_2} = \arg(r^{P}_{1-2}) \\ \Phi^{P}_{Ti} = \arg(r^{P}_{2-3}) \end{cases}, \tag{3}$$

where r^{P}_{1-2} and r^{P}_{2-3} are the amplitude Fresnel coefficients (see chap. I of [45]) for an electromagnetic field of polarization P reflected respectively at the Air/TiO_2 interface and at the TiO_2/Ti interface. As we neglect a possible imaginary part of n_{TiO_2}, $\Phi^{P}_{TiO_2}$ is equal to 0 or $\boldsymbol{\pi}$, depending on the light polarization and on the light incidence angle. The value of Φ computed in Equation **(2)** is an average over the phase-shift for TE and TM polarizations. This equation remains strictly valid in the case where the TE and TM components of the non-polarized incident light keep the same amplitude after reflection. This is particularly not the case close to the Brewster angle of the air/TiO_2 interface, which is of about 70°. A systematic study of the validity of Equation **(2)** as a function of the incidence angle is beyond the scope of this paper. Nevertheless, to ensure a correct validity of this equation, the highest value of the incidence angle has been limited to 45° in the present study. Typical values of Φ for the samples studied here lie between 89° for a wavelength of 350 nm and 36° for a wavelength of 800 nm.

When the interfaces phase-shift is neglected, that is when $\Phi = 0$, the formulas giving the oxide thickness e from the reflectance spectra minima and maxima positions are the followings:

$$\begin{cases} \text{for a wavelength position } \lambda_{max} \text{ of a maximum:} \\ \qquad e = \dfrac{2m\pi \times \lambda_{max}}{4\pi n_{TiO_2}\cos(\theta_r)} \quad m \in \mathbb{N}^* \\ \text{for a wavelength position } \lambda_{min} \text{ of a minimum:} \\ \qquad e = \dfrac{(2m+1)\pi \times \lambda_{min}}{4\pi n_{TiO_2}\cos(\theta_r)} \quad m \in \mathbb{N} \end{cases}. \tag{4}$$

The oxide thickness won't be perfectly constant on real samples: equation **(1)** and **(4)** will thus give an average value of the oxide layer thickness on the illuminated area of the sample.

3. Experimental details

3.1. Samples preparation

Six samples were cut out from a 1 mm thick on ASTM Grade 2 titanium sheet. Two different series of three mirror polished samples were prepared with two different roughness levels. The first mirror polished series referred to as "Alumina" has been obtained by a complete mechanical polishing. The second series designated as "Vibromet" was further polished in a vibratory polisher. All samples were polished separately, one by one. The roughness of the samples has been characterized by the S_a roughness parameter [46] defined as:

$$S_a = \frac{1}{A}\iint_A |Z(x,y)|dxdy\,,$$

where A is the characterized area on the sample and $Z(x,y)$ the height of the position (x,y) relatively to the average height of the area A. It corresponds to the arithmetic average of the absolute difference in height of each point compared to the mean height of the surface. The typical roughnesses of the "Alumina" and "Vibromet" series samples correspond respectively to S_a parameters of about 60 nm and 15 nm. As the model material of Figure 1 assumes perfectly flat interfaces, two substrates with two different roughness levels have been prepared, in order to check a potential influence of the sample roughness on the results. The roughness of the roughest series was limited by the ellipsometry technique, which doesn't work for too rough samples.

The samples were anodized in a galvanostatic regime by imposing a current density equal to 20 mA/cm². The counter electrode is circular and made of activated titanium. All experiments were performed in a 0.5 M sulfuric acid electrolytic solution (H_2SO_4) at room temperature. The cell potential increases gradually during the anodizing process. When the potential reaches a desired value, the current is shut down and the sample is removed from the bath. Three different maximum cell potentials values have been chosen: 10 V, 20 V and 90 V. Figure 2 is a picture of the six samples prepared in the present study. The samples exhibit different interferential colors due to different

oxide thicknesses. For a same maximum cell potential, the two series don't exhibit the same colors. This is due to the influence of the substrate roughness on the oxide layer growth.

Figure 2: Picture of the six samples considered in the present study with the value of the maximum cell potential for each sample.

3.2. Samples characterization

3.2.1. Ellipsometric characterizations

Ellipsometric measurements have been carried out on the anodized samples at three different angles (65°, 70° and 75°) with a phase modulation ellipsometer, Horiba Jobin Yvon UVISEL®. To describe the spectral behavior of the refractive indexes, the new amorphous dispersion model [47] was used for the oxide layer and the classical dispersion model [48] was used for the titanium substrate. The sample is represented as a four-layer material in the ellipsometric model, as described in Figure 3. A similar model has been used by Skrowronski et al. [49] to determine the refractive indexes and thicknesses of TiO_2/Ti/glass multilayer systems obtained by gas injection magnetron sputtering. The first layer is the titanium substrate, assumed to have an infinite thickness. The second layer is the interface between the titanium substrate and the titanium oxide layer and its thickness is denoted as L_1. This layer represents a transition layer between the substrate and the oxide, considered here as substrate "roughness" and is considered as a composite material, made of 50% Ti and 50% oxide in volume fraction. The third layer is the oxide layer which thickness is denoted as L_2. To consider a potential porosity of the oxide layer, this layer is considered as a composite material made of $(100 - X)\%$ oxide and $X\%$ Air in volume fraction. The fourth layer, which thickness is denoted as L_3, corresponds to the oxide layer "roughness". It is modeled as a mixed material composed of 50% air and 50% oxide in volume fraction. It is important to notice that all the ellipsometric model parameters were adjusted at the same time on the six samples and for the three angles. The titanium substrate is considered the same (same refractive index) for all samples. The oxide material is

considered the same for all the samples. When the refractive index value drops in layer L_2, the model adjusts the porosity factor X. The refractive index of all composite layers is computed through the effective medium Bruggeman theory [50]. Note that we don't exactly compute here the refractive index of TiO_2, but the refractive index of the oxide layer, which could for example include impurities or porosities. As the ellipsometric model parameters were adjusted at the same time on the six samples, a non-zero value for X indicates a decrease of the oxide layer refractive index compared to the other samples, attributed here to an increase of the oxide layer porosity. In addition, a zero value for X doesn't mean that the oxide layer isn't porous.

Figure 3 : Representation of the four-layer ellipsometric model with the different layer thicknesses.

3.2.2. Transmission electron microscope images of foils cut out with a Focused Ion Beam

Direct measurements of the thickness of the oxide layer were carried out by transmission electron microscopy, by imaging lamellae of the samples. The lamellas preparations were achieved in a Field Electron and Ion Helios 600i dualbeam (focused Gallium (Ga) ions beam and field emission gun-scanning electron microscopy electrons column) workstation. First, a Platinum (Pt) protective layer was deposited on the sample surface. Then, few microns deep cross sections were milled on both sides of the Pt deposit. The lamellas were lift out and slid on a copper grid. The lamellas were thinned with the Ga ion beam until a thickness of about 100 nm. A low kV (5 kV) cleaning was finally applied on both sides of the lamellas, in order to remove most of the surface layer damaged by the ion beam. The length of the thin part of the lamellas was of a few microns. Thereafter, inside the dualbeam, images were acquired with a Scanning Transmission Electron Microscope (STEM) detector along the thin part of the lamella. The STEM detector is made of several concentric parts. The images were acquired with the intermediate part of the annular detector. The acceleration voltage was 30 kV.

3.2.3. Reflectance characterizations

The samples reflectance measurements have been carried out in the specular direction (i.e. with an observation angle equal to the incidence angle) at two different incidence angles: 15°, 45°. The measurements have been performed on a goniospectrophotometer, which is described in details in references [51,52]. This device has been designed to perform Bidirectional Reflectance Distribution Function (BRDF) measurements. However, in the present case, the samples are mirror polished and the typical angular width of their BRDF is far below the goniospectrophotometer angular resolution. The goniospectrophotometer is thus used here to measure total reflectance, that is the ratio of the total light flux reflected by the sample over the incident light flux. The reflectance measurements are performed on the wavelength range [350 nm – 800 nm] with non-polarized light. The illuminated area on the samples is elliptical and depends on the incidence angle. The minor axis of the ellipse is 1 cm long, whereas the major axis has a length equal to $1\ \mathrm{cm}/\cos(\theta_i)$, that is, about 1 cm for an incidence angle of 15° and about 1.4 cm for an incidence angle of 45°.

4. Results

4.1. Oxide layer thickness

4.1.1. Ellipsometric characterizations

The X porosity factor of the oxide layer deduced from the ellipsometric model is presented in Table 1. This factor is equal to zero for all samples anodized at maximum cell potentials of 10 V and 20 V and increases for the samples anodized at maximum cell potentials of 90 V. As mentioned previously, this doesn't mean that the oxide layer of the 10 V and 20 V samples isn't porous, but this means that any residual porosity of the oxide layer is included in the oxide layer refractive index value.

The ellipsometric parameters $\boldsymbol{L_1}$, $\boldsymbol{L_2}$ $\boldsymbol{L_3}$ obtained for the 6 samples considered here are presented in Table 2, as well as the total oxide thickness $L_1 + L_2 + L_3$, which takes into account the transition

layers L_1 and L_3. We can observe an increase of the total oxide layer thickness with the maximum cell potential. Also, for the same maximum cell potential, the samples of the Alumina series exhibit oxide thicknesses higher than the samples of the Vibromet series, which explains the color difference observed in Figure 2, particularly for the samples anodized at maximum cell potentials of 10 V and 20 V. The L_1 (substrate – oxide) transition layer thickness represents between 9% to 20% of the total oxide thickness. The L_3 (oxide – air) transition layer thickness represents generally between 4% to 6% of the total oxide thickness, except for the 10 V anodized sample were it represents 30% of the oxide thickness.

Table 1: ***X*** porosity factor of the oxide layer deduced from the ellipsometric model.

Table 2: Ellipsometric parameters $\boldsymbol{L_1}$, $\boldsymbol{L_2}$ $\boldsymbol{L_3}$ and the total oxide layer thickness $\boldsymbol{L_1 + L_2 + L_3}$ for the different samples.

4.1.2. Transmission electron microscope images of foils cut out with a Focused Ion Beam

FIB lamellas were prepared from two samples of the Vibromet series: the samples anodized at maximum cell potentials of 20 V and 90 V. The 10 V sample has an oxide layer too thin to be observed through this technique. STEM images of theses lamellas are presented on Figure 4. On each image, 20 measurements of the oxide thickness have been performed on different positions. Figure 4 shows the averages and the standard deviations over these measurements: an oxide thickness of 31 ± 3 nm has been measured on the 20 V sample, and an oxide thickness of 163 ± 22 nm has been measured on the 90 V sample. The thickness standard deviation represents 10% of the thickness value for the 20 V sample, and 13% for the 90 V sample. The oxide thickness measurement uncertainty is due to the uncertainty in determining the top and bottom edges of the layer on the image, as well as to oxide thickness variations inside the observed area. The oxide thickness variations are clearly visible for the 90 V sample (Figure 4 (b)). It can be also observed

that, in both cases, the oxide layer isn't homogeneous. Both oxide layers seem to present porosities, here shown as dark areas inside the oxide layer in these dark field images. When looking in detail at the oxide layer of the 90 V Vibromet sample, it can be observed that the layer can be split into three sublayers, with two thin homogeneous sublayers surrounding a third bigger porous one. The contrast and resolution of the images is for now too bad to estimate properly the thicknesses of these sublayers. The acquisition of new TEM images of the FIB lamellae with higher resolution are planned, to compare the thicknesses of these sublayers with the thicknesses obtained with the ellipsometric model (Table 2). Also, as observed in Table 1, the X porosity factor increases with the maximum cell potential, and thus with the time spent in the electrolytic bath. This could lead to a non-homogeneous spreading of the porosities inside the oxide layer, which is not observed in Figure 4. More resolved electronic images of the FIB lamellae could reveal this phenomenon. Note that rapid Transmission Kikuchi Diffraction (TKD) analyzes have shown small islands of anatase crystalline TiO_2 inside the oxide layer for the 90 V sample, whereas no crystalline islands where observed for the 20 V sample.

Figure 4: STEM images of FIB lamellas cut out from the samples anodized at maximum cell potentials of (a) 20 V and (b) 90 V from the Vibromet series. The oxide thicknesses have been measured on 20 different positions on the images. The averages and the standard deviations over these measurements are shown on each figure.

4.1.3. Reflectance measurements

Figure 5 shows the spectral specular reflectances of the Vibromet series samples, at the two different incidence angles 15° and 45°. The local extrema of these reflectance spectra have been used to characterize the oxide thickness of the samples. The 10 V and 20 V samples reflectance spectra exhibit for example one local minimum at all angles, which corresponds to an interference order $m = 0$. The 90 V sample reflectance spectra exhibit one local minimum ($m = 1$) and one local maximum ($m = 2$) at all angles. Note that the local extrema positions vary with the measurement angle, with a shift of the extrema positions towards the « blue wavelengths » when the angle

292 increases. The oxide thickness of one sample is computed as following: oxide thickness values are
293 computed for all angles and all local extrema positions through equations **(3)** or **(4)**, and then an
294 average is taken over these values. The titanium and oxide layer refractive indexes at the extrema
295 positions are extracted from the ellipsometric measurements (see Figure 6 and Figure 7 below). For
296 both 90 V samples, which have a non-zero X porosity factor (see Table 1), the decrease of the oxide
297 layer refractive index is taken into account through the Bruggeman [50] theory. Note that, as
298 mentioned previously, our oxide layer thickness calculations don't take into account the imaginary
299 part of the TiO_2 refractive index, which is always smaller than 0.1i (see Figure 7(b)) for all extrema
300 positions considered here. Table 3 shows the oxide thickness of the different samples, computed
301 from the reflectance spectra extrema, when the interfaces electromagnetic phase-shift is taken into
302 account and when this phase-shift is neglected (see equations **(3)** and **(4)**). The values indicated in
303 brackets in Table 3 correspond (in % relatively to the average value) to the bias corrected standard
304 deviation over the values obtained for the different angles and the different extrema positions: this
305 standard deviation exhibit very low values. It can be observed, particularly for the samples anodized
306 at maximum cell potentials of 10 V and 20 V, that the oxide thickness can be the same order of
307 magnitude as the S_a roughness parameter of the substrate (see section 3.1). S_a is measured on an area
308 of about 1 mm^2, which corresponds to a macroscopic scale. Nevertheless, a high value of S_a doesn't
309 prevent the oxide thickness to be locally well defined, and thus to generate the interference
310 phenomenon leading to the reflectance spectra extrema. For example, on Figure 4(a), for the 20 V
311 sample, the oxide layer thickness variations are lower than 3 nm, which is very low compared to the
312 S_a roughness parameter value of 15 nm for this sample. Variations in the oxide thickness in the same
313 order of magnitude as the oxide thickness itself would also lead to a complete blurring of the
314 interference fringes, which is not observed in Figure 5.
315
316 **Figure 5**: Measured spectral specular reflectances of the Vibromet series at the two different angles
317 15° and 45° on the wavelength range [350 nm – 800 nm].

Table 3: Oxide layer thicknesses of the different samples computed from the reflectance spectra extrema positions when the interfaces electromagnetic phase-shift is considered and when this phase-shift is neglected. The values indicated in brackets correspond to the bias corrected standard deviation over the values obtained for the different angles and the different extrema positions and are computed in % relatively to the average value.

5. Discussion

5.1. Comparison of the refractive indexes measured through ellipsometry and literature results

5.1.1. Titanium refractive index

Figure 6 presents the real and imaginary parts of the titanium refractive index on the wavelength range [200 nm – 900 nm] measured through our ellipsometric characterizations. Our measurements have been compared to four different references : Joseph et al. [29], Lynch et al. [53], Blondeau et al. [54] and Musa et al. [55]. For the refractive index real part, we observe a relatively good agreement between our measurements and these of Blondeau et al.. Other measurements from Joseph et al. and Musa et al. are relatively close to ours, but a higher discrepancy is observed with these from Lynch et al.. For the imaginary part, our measurement is not particularly close to one of the literature measurements. Joseph et al., Lynch et al. and Musa et al. are close to each other, whereas a higher discrepancy is observed with Lynch et al. Our measurement lies in-between Lynch et al. and the other ones.

Figure 6: (a) Real and (b) imaginary parts of Titanium refractive index on the wavelength range [200 nm – 900 nm]. The results obtained by our ellipsometric measurements have been compared to four different references : Joseph et al. [29], Lynch et al. [53], Blondeau et al. [54] and Musa et al. [55].

The samples studied by Joseph et al. and Blondeau et al. are close to our experimental conditions, which explains that their refractive indexes are close to ours. Joseph et al. characterized through

346 ellipsometry 99.9% pure titanium samples covered with anodically grown oxide films. Blondeau et
347 al. fit reflectance spectra of a set of titanium samples (no more information is given on the raw
348 material in reference [54] but another publication by the same team [56] mention 99.7% pure
349 titanium) anodized in sulfuric acid at different voltages. The samples studied by Musa et al. and
350 Lynch et al. aren't anodized ones. Musa et al. measured through ellipsometry the refractive index of
351 99.9% pure titanium samples. The measurements are performed in air and might be influenced by a
352 potential oxide layer at the samples surface. Lynch et al. characterized samples, which were spark cut
353 from polycrystalline ingots (no more details are given on the material type). They employed two
354 different techniques to measure the optical properties of the samples : reflectance measurements and
355 a calorimetric technique [57]. The real and imaginary parts of the titanium refractive index are then
356 deduced thanks to a Kramers-Krönig analysis [58,59], which might explain the higher discrepancy
357 observed between their measurements and the other ones extracted from the literature. Note that their
358 samples are exposed to air for 2-3 min, but no correction has been made to take into account a
359 potential oxide layer at the surface sample.

360 **5.1.2. Oxide layer refractive index**

361 The oxide layer refractive indexes obtained from the ellipsometric measurements are compared to
362 literature values for titanium samples anodized in conditions similar to ours. Figure 7 presents the
363 real and imaginary parts of the oxide layer refractive index on the wavelength range [200 nm – 900
364 nm]. Two different cases are presented. The first one, with the X porosity factor of the oxide layer
365 equal to 0% corresponds to all samples anodized at 10 V and 20 V. The second one, with $X = 13\%$,
366 corresponds to the 90 V anodized sample from the Alumina series (see Table 1). Our measurements
367 have been compared to different references: Joseph et al. [29], the two different results presented by
368 Van Gils et al. in [37] for samples anodized at 10 V and 80 V, the two different results presented by
369 Blondeau et al. in [60] (for the case of titanium samples anodized in 0.5 M H_2SO_4) and attributed to
370 amorphous and anatase TiO_2, and the two different results presented by Diamanti et al. in [8] for

samples anodized at 60 V and 90 V. The principal preparation conditions of the samples which oxide layer refractive index values are presented in Figure 7 are summarized in Table 4.

Table 4: Principal preparation conditions for the samples which oxide layer refractive index values are presented in Figure 7.

Figure 7: (a) Real and (b) imaginary parts of oxide layer refractive index on the wavelength range [200 nm – 900 nm]. The results obtained by our ellipsometric measurements with two different values of the oxide layer ***X*** porosity factor (0% and 13%) have been compared to different references : Joseph et al. [29], the two different results presented by Van Gils et al. in [37] for samples anodized at 10 V and 80 V, the two different results presented by Blondeau et al. in [60] (for the case of titanium samples anodized in 0.5 M H_2SO_4) and attributed to amorphous and anatase TiO_2 and the two different results presented by Diamanti et al. in [8] for samples anodized at 60 V and 90 V. Diamanti et al. and Van Gils et al. didn't take into account the imaginary part of the oxide layer refractive index.

For the refractive index real part, our results lie in between Diamanti et al. and the 10 V sample of Van Gils et al. Our case $X = 0\%$ is close to the anatase case of Diamanti et al. in the wavelength range [380 nm – 500 nm]. Most references observe a global decrease of the oxide layer refractive index real part with wavelength. For the refractive index imaginary part, our results are lower than the other references, with an imaginary part equal to zero for wavelengths higher than 400 nm. We observe only a slight influence of X on the refractive index imaginary part. All references have almost the same global shape.

Contrary to references [8,37,60] and the present work, Joseph et al. [29] presented a unique refractive index value for all their samples. They actually compared the refractive index values obtained first by using only the eight thinnest films and then by using only the eight thickest films: the results obtained are identical, meaning that, contrary to other publications they didn't observe an influence of the anodizing voltage on the oxide layer refractive index. Note that their maximum anodizing voltage (40 V) is lower than other publications. The refractive index measured by Joseph et al. is higher than these of the present study. Contrary to the present work, their samples were anodized using a mixed method of galvanostatic control and then potentiostatic control for a period of 30 min. In the present case, the anodizing process is stopped just after the galvanostatic growth,

401 which could lead to a more porous oxide layer. The STEM images of Figure 4 tend to show that the
402 oxide layer of the present study is porous, which confirms this assumption.

403 Blondeau et al. [60] also get refractive indexes higher than the present study. Their samples were
404 anodized under either potentiostatic conditions for anodizing voltages lower than 50 V or
405 galvanostatic conditions otherwise, as explained in [56]. Again, the potentiostatic anodizing could
406 explain that Blondeau et al. obtained less porous oxide layers that the present study. Blondeau et al.
407 showed with electron diffraction characterizations, that the oxide films obtained at voltages higher
408 than 50 V correspond to well-crystallized anatase TiO_2. However, for lower voltages, the oxide films
409 exhibited only a short-range crystalline order, and are thus considered as "quasi-amorphous". This is
410 accordance with the TKD analyzes of our FIB lamellae were small islands of anatase crystalline
411 TiO_2 have been observed inside the oxide layer for the 90 V sample, whereas no crystalline islands
412 where observed for the 20 V sample. Blondeau et al. computed two different oxide layer refractive
413 index values, one for the "amorphous" sample set (anodizing voltage in the range [1 V – 48 V]), and
414 the second one for the "anatase" sample set (anodizing voltage in the range [54 V – 98 V]). Contrary
415 to what have been observed for example by Bendavid et al. [61] for TiO_2 thin films deposited by
416 filtered arc deposition showing that anatase has the refractive index higher than amorphous TiO_2, the
417 anodic anatase containing oxide studied by Blondeau et al. exhibits a refractive index lower than
418 their anodic amorphous oxide. This leads to believe that Blondeau et al. samples anodized at higher
419 voltages have a more porous oxide layer than those anodized at lower voltages. This is in accordance
420 with our observations of an increase of the porosity factor X of our ellipsometric model for samples
421 anodized at 90 V (see Table 1).

422 The anodizing conditions of Diamanti et al. [8] are similar to these of the present study
423 (galvanostatic process with a current density of 20 mA/cm^2), which is coherent with the fact that
424 their oxide layer refractive index values are the closest to ours. The refractive index values measured
425 by Diamanti et al. remain nevertheless globally higher than the present study. X-ray diffraction

426 characterizations showed that the oxide layer is amorphous for the 60 V anodized sample, whereas it
427 exhibited an anatase phase in the case of the 90 V anodized sample, which is again in accordance
428 with the observations of the present study. As observed by Blondeau et al., the oxide layer refractive
429 index of the sample anodized at a high voltage is lower than the oxide layer refractive index of the
430 sample anodized at a lower voltage, suggesting again that the oxide layer porosity increases with the
431 maximum cell voltage.

432 Van Gils et al. [37] computed the oxide layer refractive index for eight anodizing voltages
433 between 10 V and 80 V. Their samples were anodized galvanostatically, with current densities of 10
434 mA/cm^2 for maximum cell voltages below 30 V and 20 mA/cm^2 for maximum cell voltages above 30
435 V. Figure 7 represents the extreme cases 10 V and 80 V, the refractive index values for intermediate
436 anodizing voltages lying in-between, with a global increase of the refractive index with the anodizing
437 voltage. This observation is in contradiction with the decrease of the oxide layer refractive index
438 observed by Blondeau et al., Diamanti et al. and the present work when increasing the maximum cell
439 voltage. A high discrepancy between the two different cases presented by Van Gils et al. is observed,
440 with very low values for their 10 V anodized sample. Van Gils et al. relate this low refractive index
441 to the formation of a microporous structure due to gas evolution during the anodizing process for a
442 low anodizing voltage. Note that their 15 V anodized sample exhibits a higher oxide layer refractive
443 index, lying in-between our values for $X = 0\%$ and $X = 13\%$, which leads to believe that the low
444 current density (10 mA/cm^2) isn't the origin of the low oxide layer refractive index value of the 10 V
445 sample. Their 80 V anodized sample has an oxide layer refractive index comparable to Joseph et al.,
446 Blondeau et al. and Diamanti et al..

447 **5.2. Estimation of the porosity of the oxide layer**

448 The porosity of the oxide layers of the 20 V and 90 V Vibromet samples has been evaluated from
449 the FIB lamellae images. The dark areas inside the oxide layer (see Figure 4) are considered as
450 porosities. The porosity is computed as the ratio of the cyan areas of Figure 8 over the total area of

451 the oxide layer, which boundaries are represented with a magenta line in Figure 8. The porosity thus
452 obtained is 16% for the 20 V Vibromet sample and 12% for the 90 V Vibromet sample. Note that
453 these values are only rough estimates of the porosity, as they are influenced by the image contrast.
454 Particularly for the 90 V Vibromet sample, the low image contrast makes it difficult to properly
455 select the dark areas inside the oxide layer, leading to an underestimation of the porosity. We can
456 thus conclude that the oxide layer porosity of the 20 V and 90 V Vibromet samples are in the same
457 order of magnitude of about 15%. This is in accordance with the ellipsometric results, where the X
458 porosity factor was also in the same order of magnitude for these samples (respectively $X = 0\%$ and
459 $X = 2\%$ for the 20 V and 90 V Vibromet samples). Electronic images of FIB lamellae of the
460 Alumina series samples are planned to confirm the good agreement between the porosity extracted
461 from the FIB lamellae images and the X porosity factor. The Alumina 90 V sample would be
462 particularly interesting for these observations, as it has an X porosity factor higher than the other
463 samples. Note that the absolute value of the X parameter of the ellipsometric model is not
464 comparable to the porosity estimated from the electronic images. The refractive index of layer L_2 in
465 the ellipsometric model is indeed an effective refractive index, average over all components of layer
466 L_2 (TiO_2, porosity, impurities…). The X parameter is thus an estimation of the relative porosity
467 between the different samples, as the refractive index of layer L_2 is estimated for all samples at the
468 same time. Different absolute values for X could thus lead to the same correct oxide layer
469 thicknesses, as long as the effective refractive index of the different layers is correctly estimated in
470 the ellipsometric model.
471
472 **Figure 8** : The same STEM images as on Figure 4 where are indicated in magenta the boundaries of
473 the oxide layer where the porosity is computed and in cyan the areas considered as porosities. (a) FIB
474 lamella of the 20 V Vibromet sample, (b) FIB lamella of the 90 V Vibromet sample.
475
476 To check if the relatively low value of the oxide layer refractive index measured by ellipsometry
477 in the present study could be explained by the porosity of the oxide layer, a second estimation of the

oxide layer porosity has been made. This estimation assumes that the difference between the maximum value of the oxide layer refractive index real part extracted from the literature and the refractive index real part measured by ellipsometry in the case $X = 0\%$ is due to air inclusions in the oxide layer. The wavelength range [400 nm – 900 nm] has been considered, as the oxide layer refractive index is almost constant in this wavelength range (see Figure 7). The amorphous case of Blondeau et al. [60] exhibits the highest values in this wavelength range, with an average value of the oxide layer refractive index real part of 2.52. The oxide layer refractive index real part measured by ellipsometry in the case $X = 0\%$ has an average value of 2.12 in wavelength range [400 nm – 900 nm]. By using the Bruggeman theory, such a refractive index decrease corresponds to a porosity of 26%, which is higher than the porosity estimated from the FIB lamellae images. The refractive index difference between the case $X = 0\%$ of the present work and Blondeau et al. amorphous case is thus only partly explained by the oxide layer porosity. Differences in the intrinsic properties of the oxide such as stoichiometry, impurities…should also be taken into account. The porosity deduced from the FIB lamellae images could also be underestimated due to insufficient contrast and/or resolution of the images. The influence of the ellipsometric model on the oxide layer refractive index should also be investigated. The oxide layer refractive index considered here corresponds indeed to the "central" part of the oxide layer (L_2 layer of the ellipsometric model), which could be "artificially" modified by the presence of the "roughness" layers L_1 and L_3.

5.3. Comparison of the oxide thickness values obtained through the different techniques

Figure 9 presents the relative variations (in %) between the oxide thickness values estimated from the reflectance spectra extrema with and without taking into account the phase-shift and, first, the average oxide thickness measured by ellipsometry and evaluated as $L_2 + (L_1 + L_3)/2$, and, second, the oxide thickness evaluated from the FIB lamellae images, have been computed. The relative variation E is here computed as the ratio of the bias corrected standard deviation over the

502 average value converted in %, which gives, in the case where we have only two different oxide
503 thickness values:

$$E(\%) = 100 \times \frac{\sqrt{(e_1 - \bar{e})^2 + (e_2 - \bar{e})^2}}{\bar{e}}, \quad (5)$$

504 where e_1 and e_2 are the two different thickness values considered to compute the variation and $\bar{e} =$
505 $\frac{e_1+e_2}{2}$.

506 **Figure 9** : Relative variation in % between the oxide thickness values estimated from the reflectance
507 spectra extrema with and without considering the electromagnetic phase-shift and, first, the average
508 oxide thickness measured by ellipsometry and evaluated as $\boldsymbol{L_2 + (L_1 + L_3)/2}$, and, second, the
509 oxide thickness evaluated from the FIB lamellae images.
510

511 The relative variations are lower than 10% for all samples in the case where the phase-shift is
512 considered. In the case where the phase-shift is neglected, the relative variations are higher than 20%
513 for the samples anodized at maximum cell potentials of 10 V and 20 V, which have oxide
514 thicknesses lower than about 50 nm. This is due to an overestimation of the oxide thickness when the
515 phase-shift is neglected. The relative variations are lower than 10% for the samples anodized at a
516 maximum cell potential of 90 V. Note that despite the difference in roughness between the Alumina
517 and Vibromet series, the same behavior of the relative variation with the maximum cell potential is
518 observed. Particularly, the relative variation is the same for the Vibromet 20 V and the Alumina 10 V
519 samples, which have the same oxide thickness.

520 It is thus observed that the error on the oxide thickness estimation made when neglecting the
521 electromagnetic phase-shift is higher for thinner oxide layers. A more systematic study of this error
522 as a function of the oxide thickness is presented in the next section.

523 **5.4. Error on the oxide thickness value when neglecting the electromagnetic phase-shift**

524 Figure 10 shows comparisons between the relative errors on the oxide thickness (determined
525 from the reflectance spectra extrema) from different origins. The relative error is computed as
526 presented in equation (5). The first origin of the relative error considered here is the electromagnetic

phase-shift. In this case, we observe that the relative error increases rapidly for small oxide thicknesses (typically below 50 nm). As observed on equation (1), two terms contribute to the oxide thickness computation. The first one is linked to the interfaces phase-shift and the second one to the interference order. Thick oxide thicknesses correspond to high interference orders. As the interfaces phase-shift doesn't depend on the interference order, the contribution of the first term decreases with the oxide thickness, explaining the decrease of the relative error with the oxide thickness. As the oxide thickness determination from the reflectance spectra extrema implies to know the oxide (and when the electromagnetic phase-shift is considered also the titanium) refractive index(es), the relative errors on the oxide thickness due to variations of the oxide refractive index real part as well as the real and imaginary parts of the titanium refractive index have been computed. By looking at the titanium and the oxide layer refractive indexes values found in the literature (see Figure 6 and Figure 7), an estimation of the maximum uncertainty on the refractive indexes has been computed. A wavelength range of [350 nm – 600 nm] has been chosen to include the positions of all extrema. Over this wavelength range, the relative variations of the titanium refractive index real and imaginary parts as well as the relative variations of the oxide layer refractive index real part have been computed for each wavelength. Then an average of these relative variations over the wavelength range [350 nm – 600 nm] is taken. The relative variations are computed the same way as for the relative error E, as the ratio of the bias corrected standard deviation over the average value. We then obtain relative variations respectively of 13%, 9% and 11% for the oxide layer refractive index real part, the titanium refractive index real part and the titanium refractive index imaginary part. A common value of 13% has then been chosen for all refractive index relative variations. The oxide layer thickness of all samples have been then recomputed for two different values of the various refractive indexes corresponding to a relative variation (as computed from equation (5)) of 13%, that is for refractive index values of $1.092n$ and $0.908n$, where n designates the refractive index value used for the oxide thicknesses computed in Table 3. The relative error on the oxide

552 thickness is then computed from these two oxide thickness values. Note that all refractive indexes
553 (real part of the oxide layer refractive index, real part of the titanium refractive index and imaginary
554 part of the titanium refractive index) have been made varied separately.
555
556 **Figure 10** : Relative error on the oxide thickness determined from the reflectance spectra extrema in
557 % as a function of the oxide thickness : (blue color) when neglecting the electromagnetic phase-shift,
558 (red color) for a relative oxide layer refractive index real part variation of 13%, (green color) for a
559 relative oxide layer refractive index real part variation of 7%, (magenta color) for a relative Ti
560 refractive index real part variation of 13%, (cyan color) for a relative Ti refractive index imaginary
561 part variation of 13%. The relative error is computed for all samples and power fit curves have been
562 added to show the evolution of the relative error with the oxide thickness.
563
564 Figure 10 shows that the error on the oxide thickness due to the uncertainty on the real and
565 imaginary parts of the titanium refractive index is negligible compared to the error due to the
566 electromagnetic phase-shift. Considering the error coming from the oxide layer refractive index real
567 part, this error is negligible compared to the error due to the electromagnetic phase-shift for oxide
568 thicknesses below 50 nm. For higher oxide thicknesses, the error coming from the oxide layer
569 refractive index real part is predominant. Nevertheless, when considering a relative uncertainty on
570 the oxide layer refractive index real part of 7% (half of the literature observed variations), the error
571 coming from the electromagnetic phase-shift remains predominant until oxide thicknesses of about
572 140 nm.

573 ## 6. Conclusion

574 The present paper estimates the oxide thickness of anodized titanium samples with three different
575 techniques: ellipsometry, FIB lamellae images and reflectance spectra extrema. . After presenting the
576 theoretical calculation of the oxide thickness from the reflectance spectra extrema, the different oxide
577 thickness values have been compared. In the case of the reflectance spectra extrema, when the phase-
578 shift encountered by the electric field reflected at the air/oxide and oxide/metal interfaces is
579 neglected, a clear overestimation of the oxide thickness is observed, particularly for samples with

oxide layers thinner than about 50 nm. The relative error on the oxide thickness when neglecting the phase-shift is indeed a decreasing function of the oxide thickness, with very high values (above 50%) for oxide layers thinner than about 20 nm. By studying the discrepancy observed in the literature for the titanium and oxide layer refractive indexes, this error has been compared to the error induced by the uncertainty on the oxide layer and substrate refractive indexes. The error induced when neglecting the electromagnetic phase-shift is predominant for oxide thicknesses below about 50 nm.

The oxide layer refractive index values measured in the present study are lower than most of the literature results. A first attempt to explain this observation has been made by estimating the oxide layer porosity from the FIB lamellae images. These preliminary results showed that porosity doesn't totally explain the low refractive index values, but further confirmations of these results are needed.

7. Acknowledgements

This work was supported by the LABEX MANUTECH-SISE (ANR-10-LABX-0075) of Université de Lyon, within the program "Investissements d'Avenir" (ANR-11-IDEX-0007) operated by the French National Research Agency (ANR).

The collaboration between Mines Saint-Etienne and Politecnico di Milano on this study was partly funded by the CMIRA program for international collaborations of Region Auvergne Rhone-Alpes.

References

[1] M. V Diamanti, B. Del Curto, M. Ormellese, M.P. Pedeferri, Photoactive and colored anodic oxides on titanium for architectural and design applications, Technical Proceedings of the 2008 Clean Technology Conference and Trade Show, 2008, 170–173.

[2] T. Dikici, S. Demirci, M. Erol, Enhanced photocatalytic activity of micro/nano textured TiO2 surfaces prepared by sandblasting/acid-etching/anodizing process, J. Alloys Compd. 694 (2017) 246–252. https://doi.org/10.1016/j.jallcom.2016.09.330.

[3] M. Fazel, H.R. Salimijazi, M. a Golozar, M.R. Garsivaz, Applied Surface Science A comparison of corrosion , tribocorrosion and electrochemical impedance properties of pure Ti

and Ti6Al4V alloy treated by micro-arc oxidation process, Appl. Surf. Sci. 324 (2015) 751–756. https://doi.org/10.1016/j.apsusc.2014.11.030.

[4] D. Prando, A. Brenna, M. Pedeferri, M. Ormellese, Enhancement of pure titanium localized corrosion resistance by anodic oxidation, Mater. Corros. 69 (2018) 503–509. https://doi.org/10.1002/maco.201709815.

[5] C. Yao, E.B. Slamovich, T.J. Webster, Enhanced osteoblast functions on anodized titanium with nanotube-like structures, J. Biomed. Mater. Res. Part A. 85A (2008) 157–166. https://doi.org/10.1002/jbm.a.31551.

[6] L. Aloia Games, A. Gomez Sanchez, E. Jimenez-Pique, W.H. Schreiner, S.M. Ceré, J. Ballarre, Chemical and mechanical properties of anodized cp-titanium in NH4H2PO4/NH4F media for biomedical applications, Surf. Coatings Technol. 206 (2012) 4791–4798. https://doi.org/10.1016/j.surfcoat.2012.03.092.

[7] I.S. Park, T.G. Woo, M.H. Lee, S.G. Ahn, M.S. Park, T.S. Bae, K.W. Seol, Effects of anodizing voltage on the anodized and hydrothermally treated titanium surface, Met. Mater. Int. 12 (2006) 505–511. https://doi.org/10.1007/BF03027751.

[8] M. V. Diamanti, B. Del Curto, M. Pedeferri, Interference colors of thin oxide layers on titanium, Color Res. Appl. 33 (2008) 221–228. https://doi.org/10.1002/col.20403.

[9] T. Wang, L. Wang, Q. Lu, Z. Fan, Changes in the esthetic, physical, and biological properties of a titanium alloy abutment treated by anodic oxidation, J. Prosthet. Dent. 121 (2018) 156–165. https://doi.org/10.1016/j.prosdent.2018.03.024.

[10] E.I. Paschalis, J. Chodosh, S. Spurr-Michaud, A. Cruzat, A. Tauber, I. Behlau, I. Gipson, C.H. Dohlman, In Vitro and In Vivo Assessment of Titanium Surface Modification for Coloring the Backplate of the Boston Keratoprosthesis, Investig. Opthalmology Vis. Sci. 54 (2013) 3863. https://doi.org/10.1167/iovs.13-11714.

[11] M.V. Diamanti, B. Del Curto, V. Masconale, M. Pedeferri, Production and Anodic Colouring

of Newly-Designed Titanium Jewels, Colour Des. Creat. 5 (2010) 16.

[12] M. V Diamanti, B. Del Curto, M.P. Pedeferri, P. Milano, Colored Titanium Oxides : From Jewelry to Biomedical Applications, Elsevier, 2018, . https://doi.org/10.1016/B978-0-12-409547-2.13581-4.

[13] L. Bartlett, An unusual phenomenon observed when anodising CP titanium to produce coloured surfaces for jewellery and other decorative uses, Opt. Laser Technol. 38 (2006) 440–444. https://doi.org/10.1016/j.optlastec.2005.06.026.

[14] A. Pérez Del Pino, P. Serra, J.L. Morenza, Coloring of titanium by pulsed laser processing in air, Thin Solid Films. 415 (2002) 201–205. https://doi.org/10.1016/S0040-6090(02)00632-6.

[15] V. Veiko, G. Odintsova, E. Vlasova, Y. Andreeva, A. Krivonosov, E. Ageev, E. Gorbunova, Laser coloration of titanium films: New development for jewelry and decoration, Opt. Laser Technol. 93 (2017) 9–13. https://doi.org/10.1016/j.optlastec.2017.01.036.

[16] A. Pérez del Pino, J.. Fernández-Pradas, P. Serra, J.. Morenza, Coloring of titanium through laser oxidation: comparative study with anodizing, Surf. Coatings Technol. 187 (2004) 106–112. https://doi.org/10.1016/j.surfcoat.2004.02.001.

[17] T. Dikici, M. Erol, M. Toparli, E. Celik, Characterization and photocatalytic properties of nanoporous titanium dioxide layer fabricated on pure titanium substrates by the anodic oxidation process, Ceram. Int. 40 (2014) 1587–1591. https://doi.org/10.1016/j.ceramint.2013.07.046.

[18] M.V. Diamanti, P. Pozzi, F. Randone, B. Del Curto, M.P. Pedeferri, Robust anodic colouring of titanium: Effect of electrolyte and colour durability, Mater. Des. 90 (2016) 1085–1091. https://doi.org/10.1016/j.matdes.2015.11.063.

[19] O.A. Galvis, D. Quintero, J.G. Castaño, H. Liu, G.E. Thompson, P. Skeldon, F. Echeverría, Formation of grooved and porous coatings on titanium by plasma electrolytic oxidation in H2SO4/H3PO4 electrolytes and effects of coating morphology on adhesive bonding, Surf.

655 Coatings Technol. 269 (2015) 238–249. https://doi.org/10.1016/j.surfcoat.2015.02.036.
656 [20] X. Fan, B. Feng, Y. Di, X. Lu, K. Duan, J. Wang, J. Weng, Preparation of bioactive TiO film
657 on porous titanium by micro-arc oxidation, Appl. Surf. Sci. 258 (2012) 7584–7588.
658 https://doi.org/10.1016/j.apsusc.2012.04.093.
659 [21] S. Cheng, D. Wei, Y. Zhou, Formation and structure of sphene/titania composite coatings on
660 titanium formed by a hybrid technique of microarc oxidation and heat-treatment, Appl. Surf.
661 Sci. 257 (2011) 3404–3411. https://doi.org/10.1016/j.apsusc.2010.11.034.
662 [22] N.K. Kuromoto, R.A. Simão, G.A. Soares, Titanium oxide films produced on commercially
663 pure titanium by anodic oxidation with different voltages, Mater. Charact. 58 (2007) 114–121.
664 https://doi.org/10.1016/j.matchar.2006.03.020.
665 [23] J.C. Marchenoir, J.P. Loup, J. Masson, ETUDE DES COUCHES POREUSES FORMEES
666 PAR OXYDATION ANODIQUE DU TITANE SOUS FORTES TENSIONS, Thin Solid
667 Films. 66 (1980) 357–369.
668 [24] Y. Serruys, T. Sakout, D. Gorse, Anodic oxidation of titanium in 1M H2SO4, studied by
669 Rutherford backscattering, Surf. Sci. 282 (1993) 279–287. https://doi.org/10.1016/0039-
670 6028(93)90934-C.
671 [25] M. Kozlowski, W.H. Smyrl, L. Atanasoska, R. Atanasoski, Local film thickness and
672 photoresponse of thin anodic TiO2films on polycrystalline titanium, Electrochim. Acta. 34
673 (1989) 1763–1768. https://doi.org/10.1016/0013-4686(89)85062-5.
674 [26] J. Michler, M. Aeberhard, D. Velten, S. Winter, R. Payling, J. Breme, Depth profiling by
675 GDOES: Application of hydrogen and d.c. bias voltage corrections to the analysis of thin
676 oxide films, Thin Solid Films. 447–448 (2004) 278–283. https://doi.org/10.1016/S0040-
677 6090(03)01105-2.
678 [27] L. Bartlett, Variability in coloured titanium surfaces for jewellery, PhD Thesis, University of
679 the Arts London, 2009.

[28] M.L. Vera, M.Á. Alterach, M.R. Rosenberger, D.G. Lamas, C.E. Schvezov, A.E. Ares, Characterization of TiO 2 Nanofilms Obtained by Sol-gel and Anodic Oxidation, Nanomater. Nanotechnol. 4 (2014) 10. https://doi.org/10.5772/58522.

[29] J. Joseph, A. Gagnaire, Ellipsometric study of anodic oxide growth: Application to the titanium oxide systems, Thin Solid Films. 103 (1983) 257–265. https://doi.org/10.1016/0040-6090(83)90442-X.

[30] R.M. Torresi, O.R. Cámara, C.P. De Pauli, M.C. Giordano, Hydrogen evolution reaction on anodic titanium oxide films, Electrochim. Acta. 32 (1987) 1291–1301. https://doi.org/10.1016/0013-4686(87)85058-2.

[31] J.F. McAleer, L.M. Peter, Photocurrent spectroscopy of anodic oxide films on titanium, Faraday Discuss. Chem. Soc. 70 (1980) 67–80. https://doi.org/10.1039/DC9807000067.

[32] F. Di Quarto, K. Doblhofer, H. Gerischer, INSTABILITY OF ANODICALLY FORMED TiO2 LAYERS, Electrochim. Acta. 23 (1978) 195.

[33] A.K. Sharma, Anodizing titanium for space applications, Thin Solid Films. 208 (1992) 48–54. https://doi.org/10.1016/0040-6090(92)90946-9.

[34] A. Karambakhsh, A. Afshar, S. Ghahramani, P. Malekinejad, Pure Commercial Titanium Color Anodizing and Corrosion Resistance, J. Mater. Eng. Perform. 20 (2011) 1690–1696. https://doi.org/10.1007/s11665-011-9860-0.

[35] M. Manjaiah, R.F. Laubscher, Effect of anodizing on surface integrity of Grade 4 titanium for biomedical applications, Surf. Coatings Technol. 310 (2017) 263–272. https://doi.org/10.1016/j.surfcoat.2016.12.038.

[36] U. Balaji, S.K. Pradhan, Titanium anodisation designed for surface colouration - Systemisation of parametric interaction using response surface methodology, Mater. Des. 139 (2018) 409–418. https://doi.org/10.1016/j.matdes.2017.11.026.

[37] S. Van Gils, P. Mast, E. Stijns, H. Terryn, Colour properties of barrier anodic oxide films on

aluminium and titanium studied with total reflectance and spectroscopic ellipsometry, Surf. Coatings Technol. 185 (2004) 303–310. https://doi.org/10.1016/j.surfcoat.2004.01.021.

[38] C. ling Yang, F. ling Chen, S. wen Chen, Anodization of the dental arch wires, Mater. Chem. Phys. 100 (2006) 268–274. https://doi.org/10.1016/j.matchemphys.2005.12.042.

[39] M.V. Diamanti, F.C. Spreafico, M.P. Pedeferri, Production of Anodic TiO2 Nanofilms and their Characterization, Phys. Procedia. 40 (2013) 30–37. https://doi.org/10.1016/j.phpro.2012.12.004.

[40] F.G. Fuhrman, F.C. Collins, Kinetics of Titanium Oxidation in Water Vapor Argon Ambient Mixtures, J. Electrochem. Soc. (1977) 1294–1299. https://doi.org/10.1149/1.2133562.

[41] A. Charlesby, J.J. Polling, The optical properties of thin oxide films on tantalum, Proc. R. Soc. London A. 227 (1954) 434–447. https://doi.org/10.1098/rspa.1955.0022.

[42] A.B. Winterbottom, Optical methods of studying films on reflecting bases depending on polarisation and interference phenomena, Trans. Faraday Soc. 42 (1946) 487–495. https://doi.org/10.1039/TF9464200487.

[43] W.A. Pliskin, Phase-shift corrections in determining the thicknesses of transparent films on reflective substrates, Solid State Electron. 11 (1968) 957–963. https://doi.org/10.1016/0038-1101(68)90115-9.

[44] Q. Cridling, INFLUENCE OF THE SUBSTRATE SURFACE PREPARATION ON OPTICAL PROPERTIES AND COLOR OF ANODIZED TITANIUM, PhD Thesis, Université de Lyon, 2018.

[45] M. Born, E. Wolf, Principles of optics : electromagnetic theory of propagation, interference and diffraction of light, Pergamon Press, 1980, .

[46] D. Whitehouse, D. Whitehouse, Profile and areal (3D) parameter characterization, Chap. 3 in: Surfaces and Their Measurement, Elsevier, 2002, 48–95. https://doi.org/10.1016/B978-190399601-0/50003-7.

[47] New Amorphous theoretical model, (n.d.). http://www.horiba.com/fileadmin/uploads/Scientific/Downloads/OpticalSchool_CN/TN/ellipsometer/New_Amorphous_Dispersion_Formula.pdf.

[48] Classical Dispersion Model, (n.d.). http://www.horiba.com/fileadmin/uploads/Scientific/Downloads/OpticalSchool_CN/TN/ellipsometer/Classical_Dispersion_Model.pdf.

[49] L. Skowronski, A.A. Wachowiak, A. Grabowski, Characterization of optical and microstructural properties of semitransparent TiO 2 /Ti/glass interference decorative coatings, Appl. Surf. Sci. 388 (2016) 731–740. https://doi.org/10.1016/j.apsusc.2016.05.159.

[50] D.A.G. Bruggeman, Berechnung verschiedener physikalischer Konstanten von heterogenen Substanzen, Ann. Phys. 24 (1935) 636.

[51] N. Matsapey, J. Faucheu, M. Flury, D. Delafosse, Design of a gonio-spectro-photometer for optical characterization of gonio-apparent materials, Meas. Sci. Technol. 24 (2013) 065901. https://doi.org/10.1088/0957-0233/24/6/065901.

[52] N. Matsapey, Rendu visuel de surfaces nano-structurées : effet de l'ordre à courte distance, PhD Thesis, Ecole Nationale Supérieure des Mines de Saint-Etienne, 2013.

[53] D.W. Lynch, C.G. Olson, J.H. Weaver, Optical properties of Ti, Zr, and Hf from 0.15 to 30 ev, Phys. Rev. B. 11 (1975) 3617.

[54] G. Blondeau, M. Froelicher, M. Froment, A. Hugot-Le Goff, Simultaneous determination of the optical indices of an absorbant film and its metallic substrate by statistical analysis of spectroreflectometric data: Application to the oxide/titanium system, Thin Solid Films. 38 (1976) 261–270. https://doi.org/10.1016/0040-6090(76)90005-5.

[55] A.H. Musa, W.E.J. Neal, OPTICAL PROPERTIES OF BULK TITANIUM AND THERMALLY GROWN OXIDE FILMS ON TITANIUM USING ELLIPSOMETRY, Surf. Technol. 11 (1980) 323–332.

[56] L. Arsov, M. Froelicher, M. Froment, A. Hugot-Le Goff, Oxydation anodique du titane en solution sulfurique : nature, épaisseur et indice de réfraction des films formés, J. Chim. Phys. 72 (1975) 275–279. https://doi.org/10.1051/jcp/1975720275.

[57] L.W. Bos, D.W. Lynch, Optical Properties of Antiferromagnetic Chromium and Dilute Cr-Mn and Cr-Re Alloys, Phys. Rev. B. 2 (1970) 4567.

[58] H.A. Kramers, La diffusion de la lumière par les atomes, Atti Cong Intern Fis. (Transactions Volta Centen. Congr. 2 (1927) 545.

[59] R. de L. Kronig, ON THE THEORY OF DISPERSION OF X-RAYS, J. Opt. Soc. Am. 12 (1926) 547–557. https://doi.org/10.1364.

[60] G. Blondeau, M. Froelicher, M. Froment, A. Hugot-Le Goff, On the optical indices of oxide films as a function of their crystallization: Application to anodic TiO2(anatase), Thin Solid Films. 42 (1977) 147–153. https://doi.org/10.1016/0040-6090(77)90411-4.

[61] A. Bendavid, P.J. Martin, H. Takikawa, Deposition and modification of titanium dioxide thin films by filtered arc deposition, Thin Solid Films. 360 (2000) 241–249.

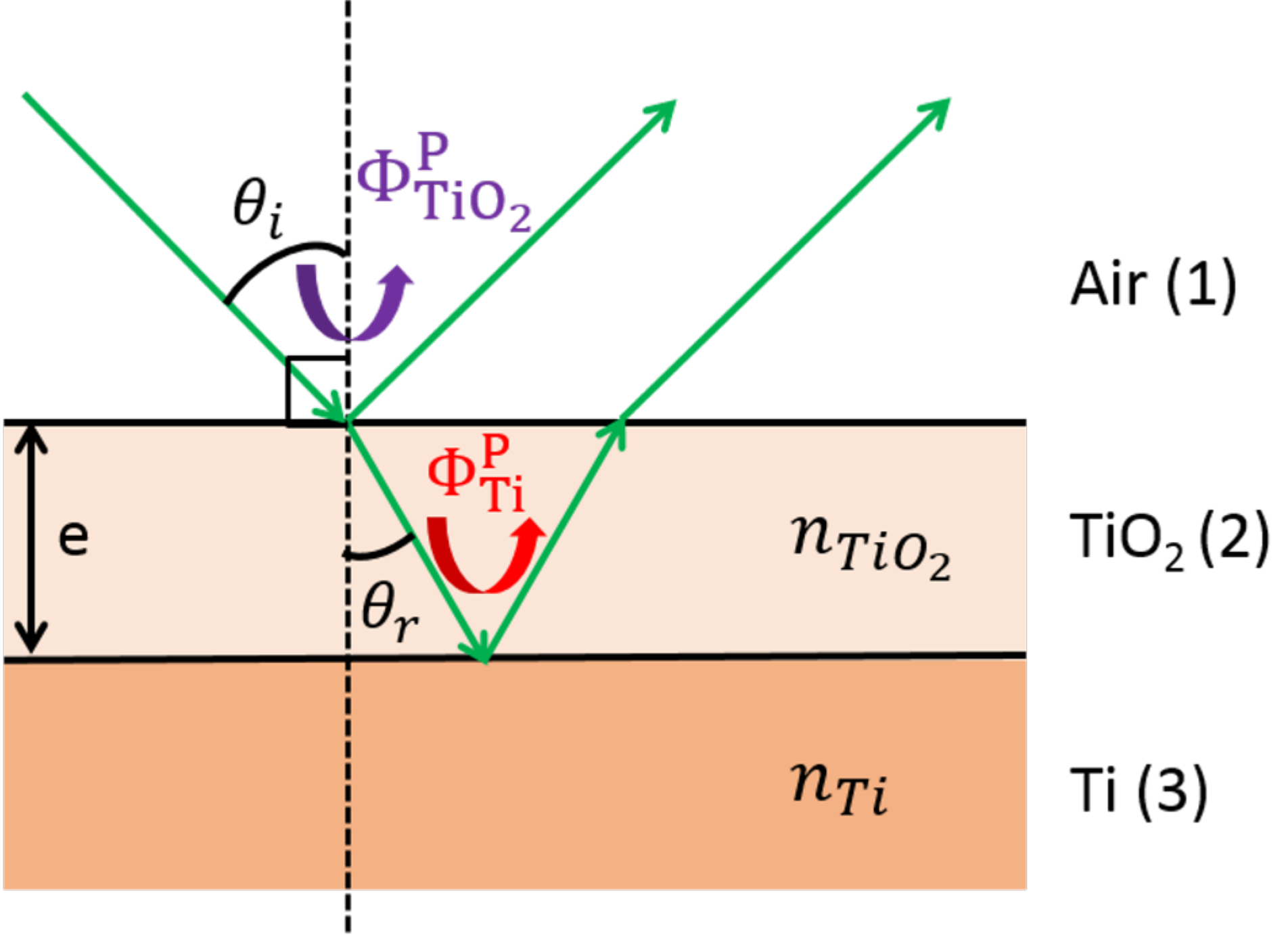
θ_i
$\Phi^{P}_{TiO_2}$
Air (1)
e
Φ^{P}_{Ti}
n_{TiO_2}
TiO_2 (2)
θ_r
n_{Ti}
Ti (3)


Alumina
10 V
Alumina
20 V
Alumina
90 V
Vibromet
10 V
Vibromet
20 V
Vibromet
90 V

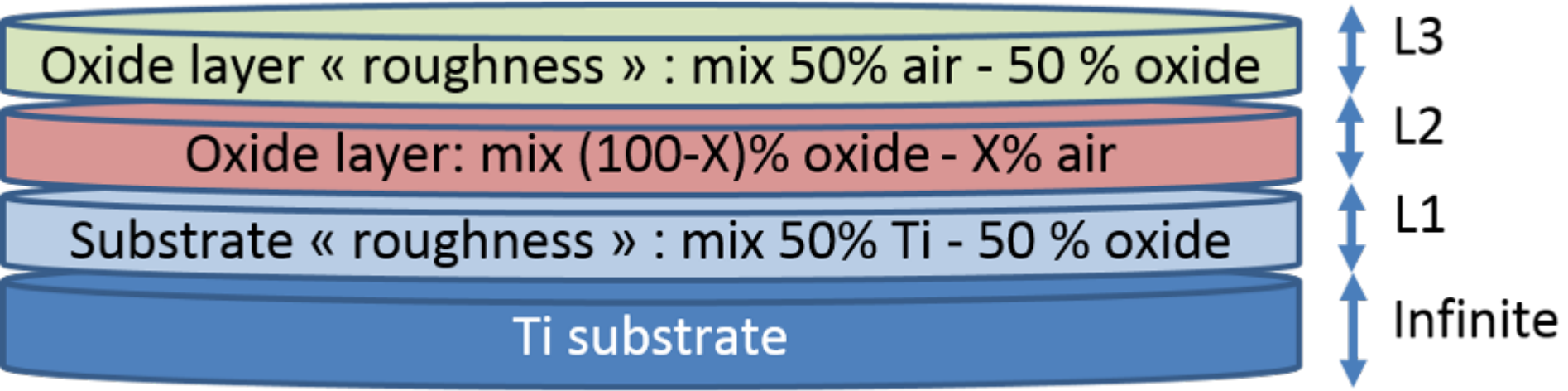
Oxide layer « roughness » : mix 50% air - 50 % oxide
Oxide layer: mix (100-X)% oxide - X% air
Substrate « roughness » : mix 50% Ti - 50 % oxide
Ti substrate
L3
L2
L1
Infinite

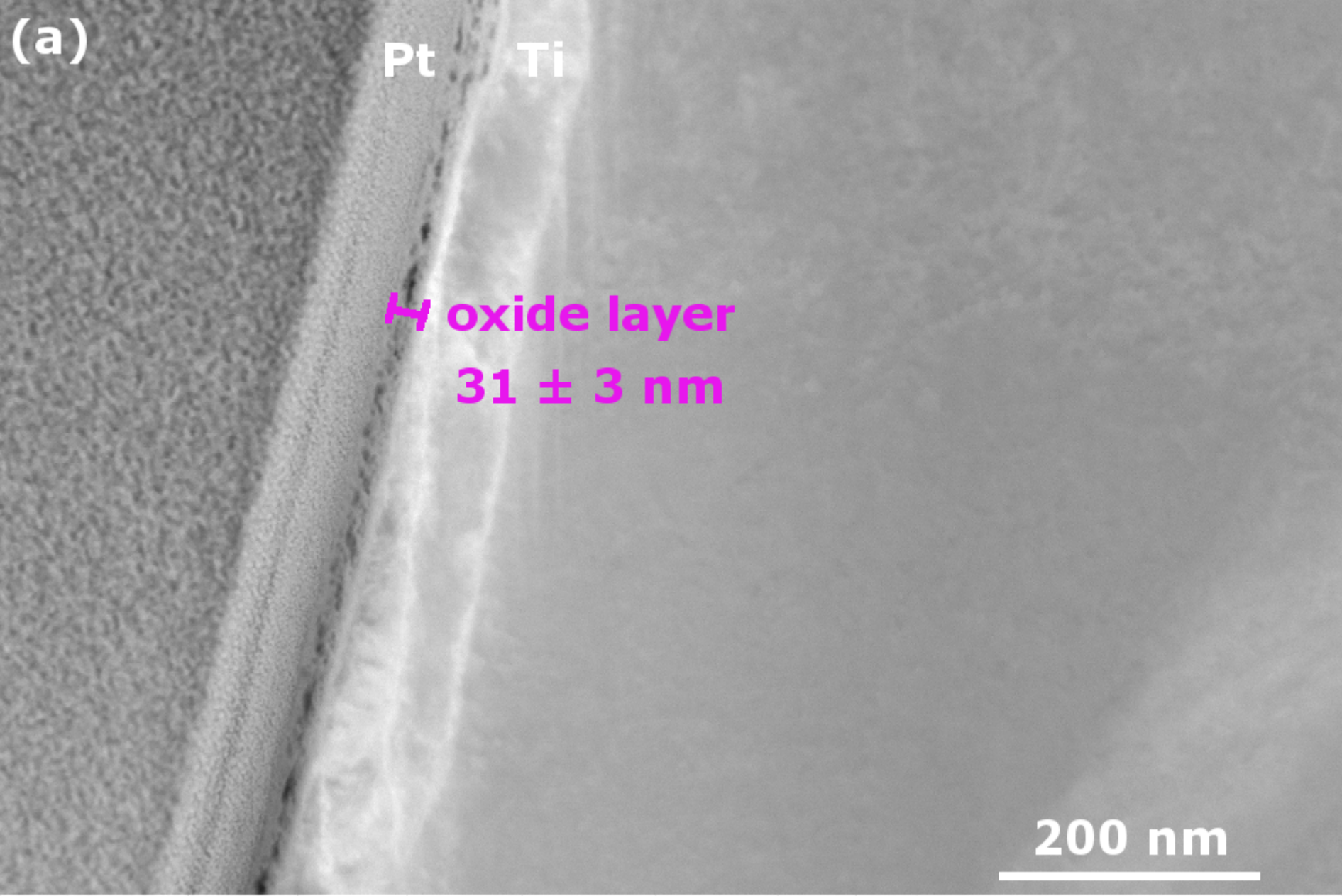
(a)
Pt
Ti
oxide layer
31 ± 3 nm
200 nm

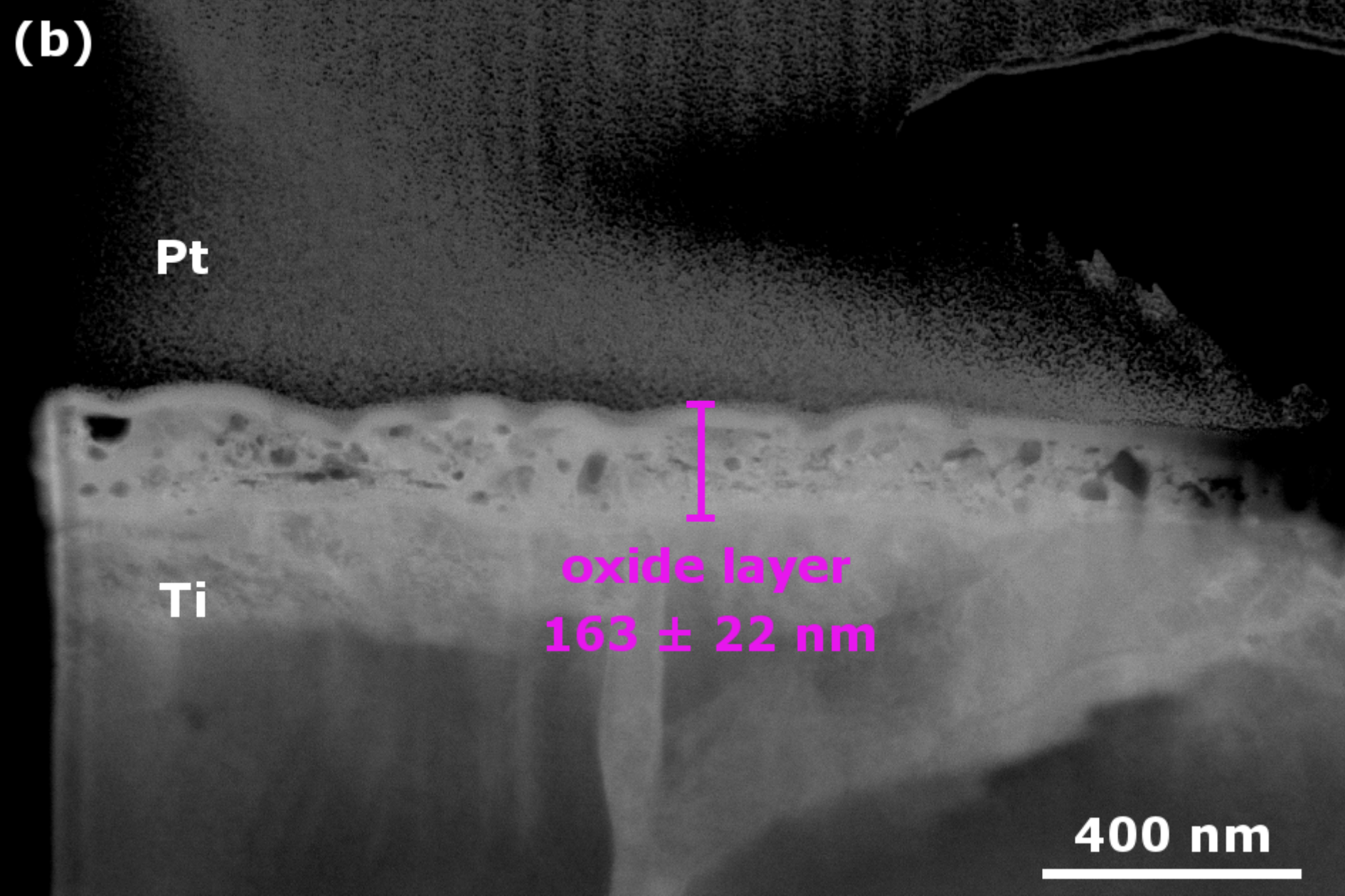
(b)
Pt
oxide layer
163 ± 22 nm
Ti
400 nm

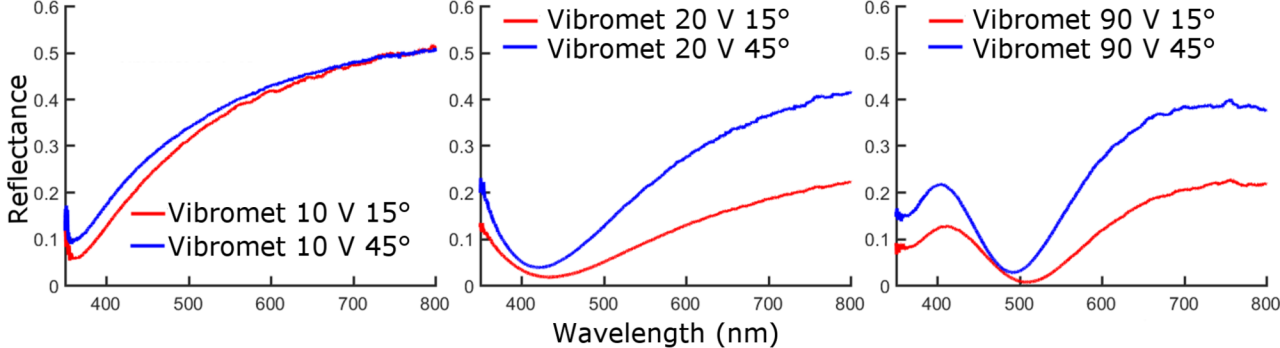
Reflectance
Wavelength (nm)
Vibromet 10 V 15°
Vibromet 10 V 45°
Vibromet 20 V 15°
Vibromet 20 V 45°
Vibromet 90 V 15°
Vibromet 90 V 45°

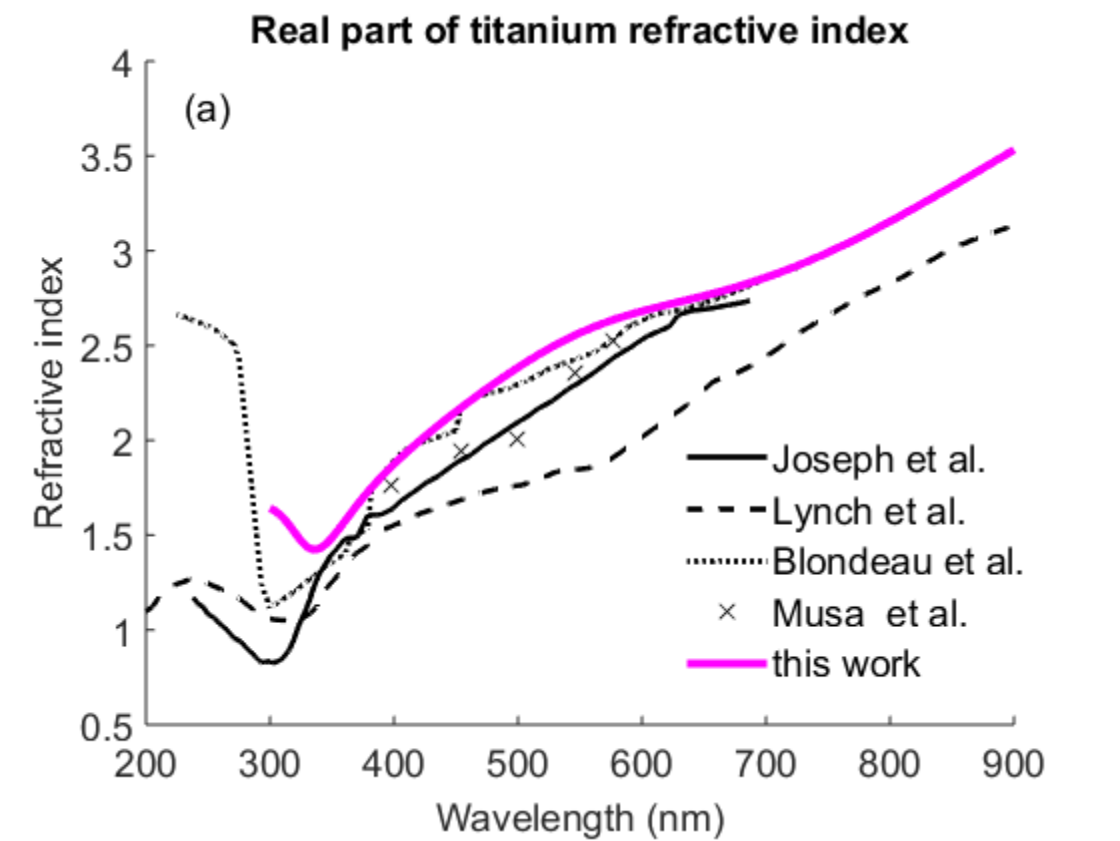
Real part of titanium refractive index
(a)
Refractive index
Wavelength (nm)
4
3.5
3
2.5
2
1.5
1
0.5
200
300
400
500
600
700
800
900
Joseph et al.
Lynch et al.
Blondeau et al.
Musa et al.
this work

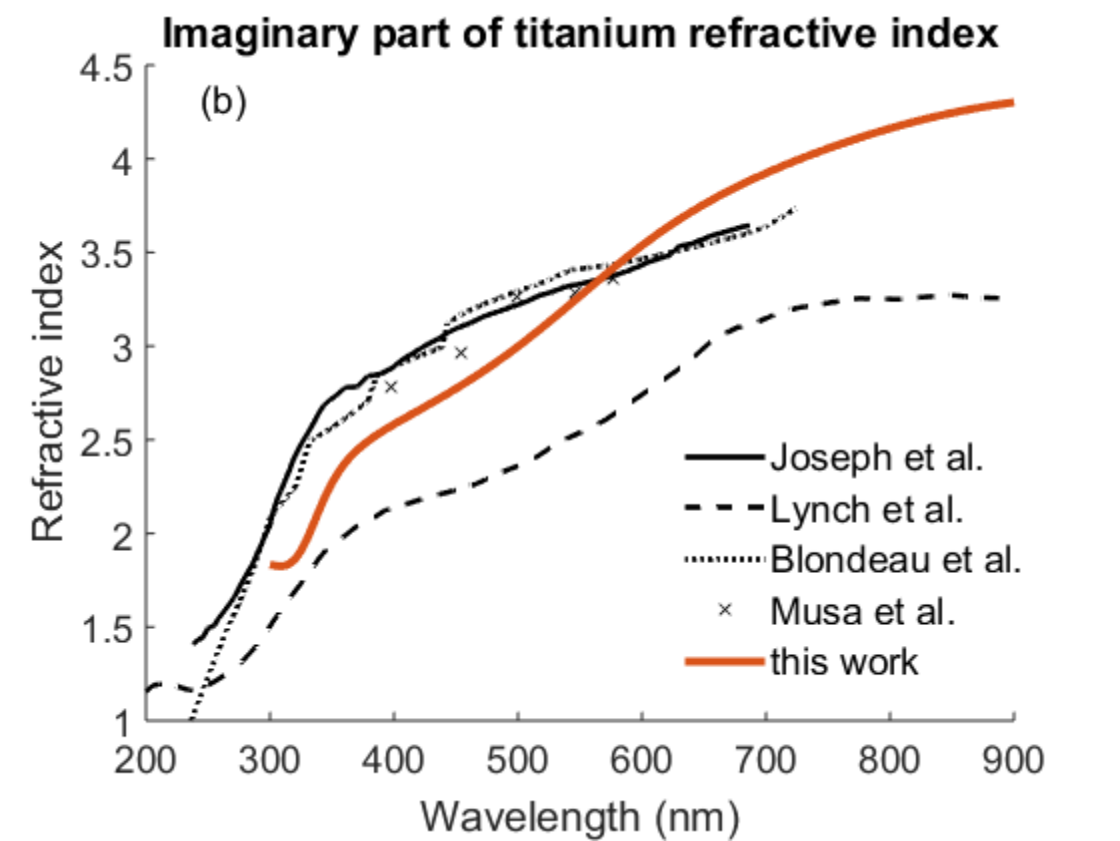
Imaginary part of titanium refractive index
(b)
Refractive index
Wavelength (nm)
4.5
4
3.5
3
2.5
2
1.5
1
200
300
400
500
600
700
800
900
Joseph et al.
Lynch et al.
Blondeau et al.
Musa et al.
this work

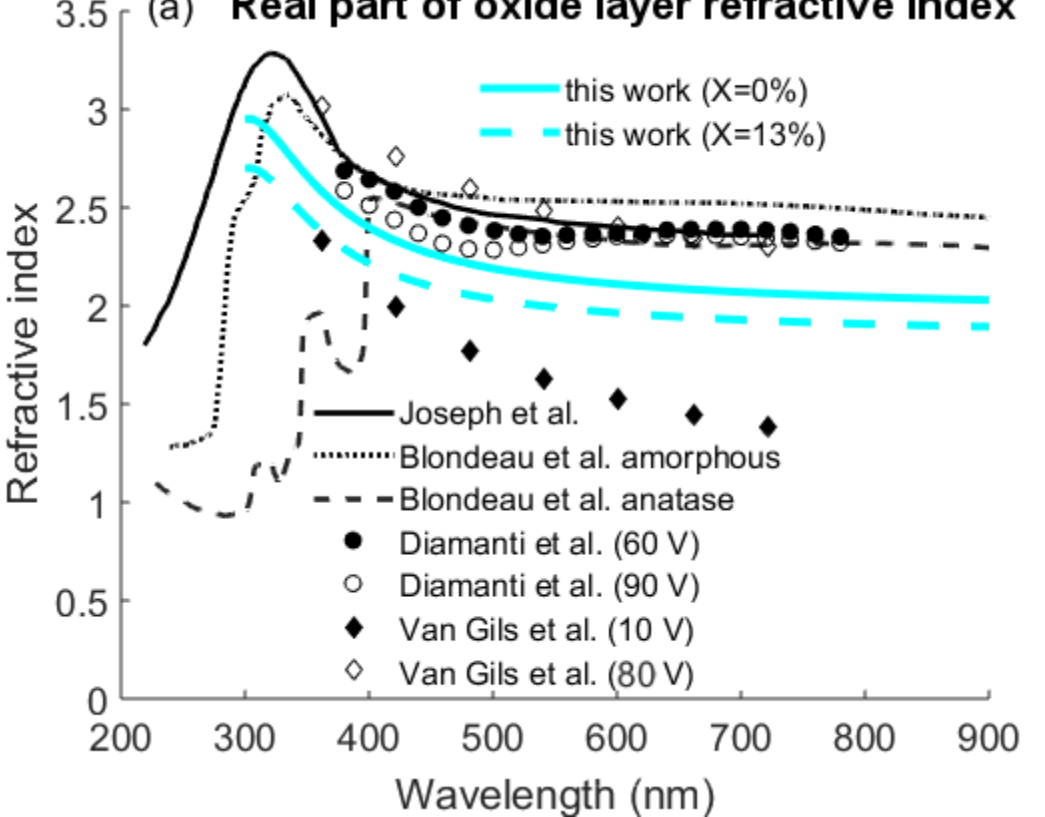
(a) Real part of oxide layer refractive index
this work (X=0%)
this work (X=13%)
Joseph et al.
Blondeau et al. amorphous
Blondeau et al. anatase
Diamanti et al. (60 V)
Diamanti et al. (90 V)
Van Gils et al. (10 V)
Van Gils et al. (80 V)
Refractive index
Wavelength (nm)
3.5
3
2.5
2
1.5
1
0.5
0
200
300
400
500
600
700
800
900

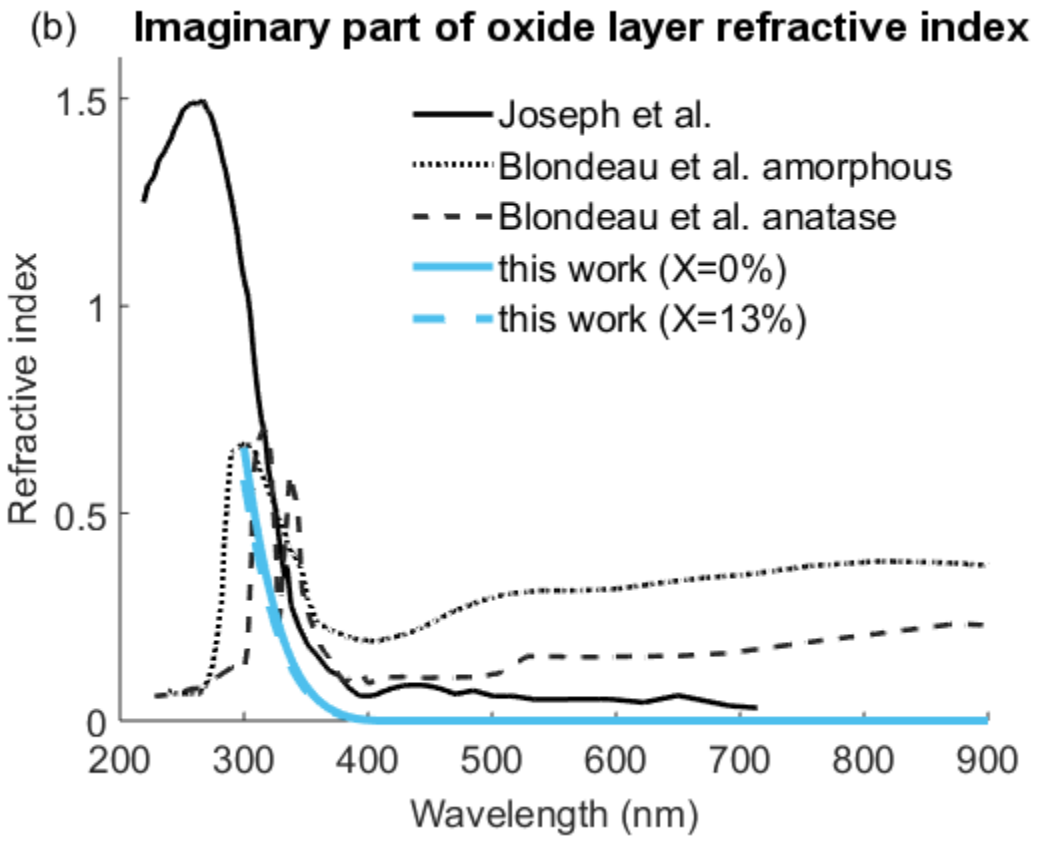
(b)
Imaginary part of oxide layer refractive index
Joseph et al.
Blondeau et al. amorphous
Blondeau et al. anatase
this work (X=0%)
this work (X=13%)
Refractive index
1.5
1
0.5
0
200
300
400
500
600
700
800
900
Wavelength (nm)

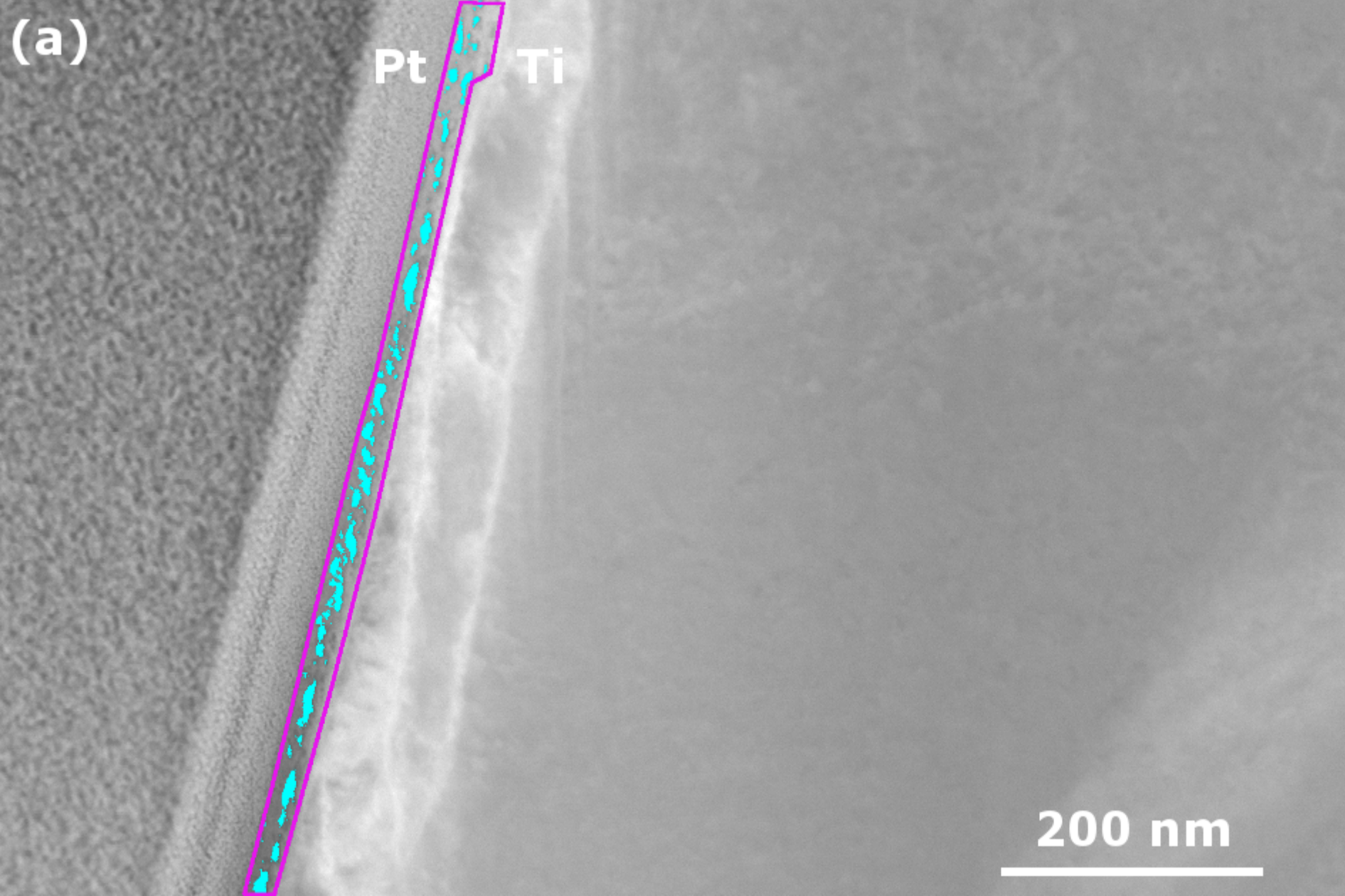
(a)
Pt
Ti
200 nm

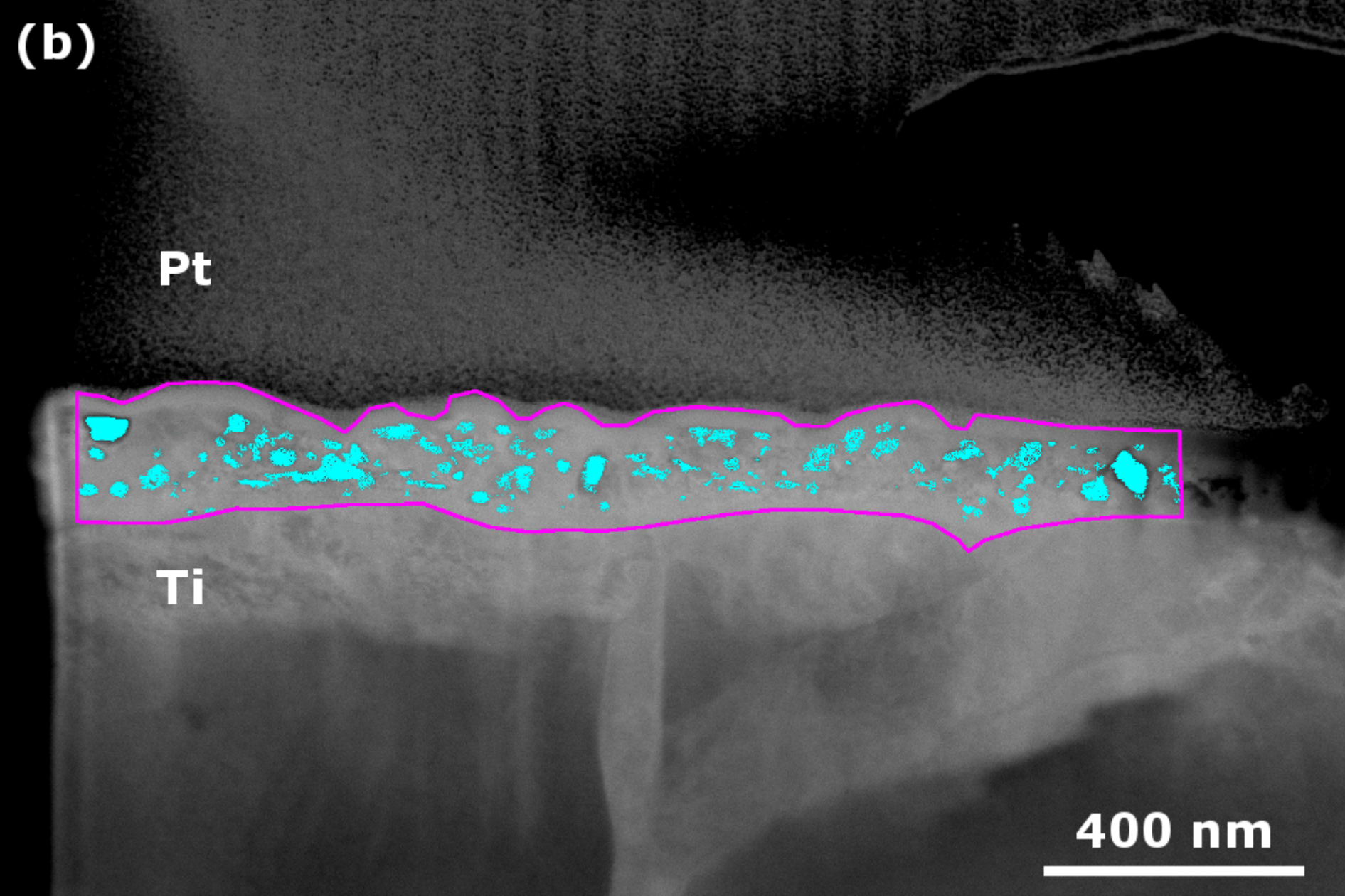
(b)
Pt
Ti
400 nm

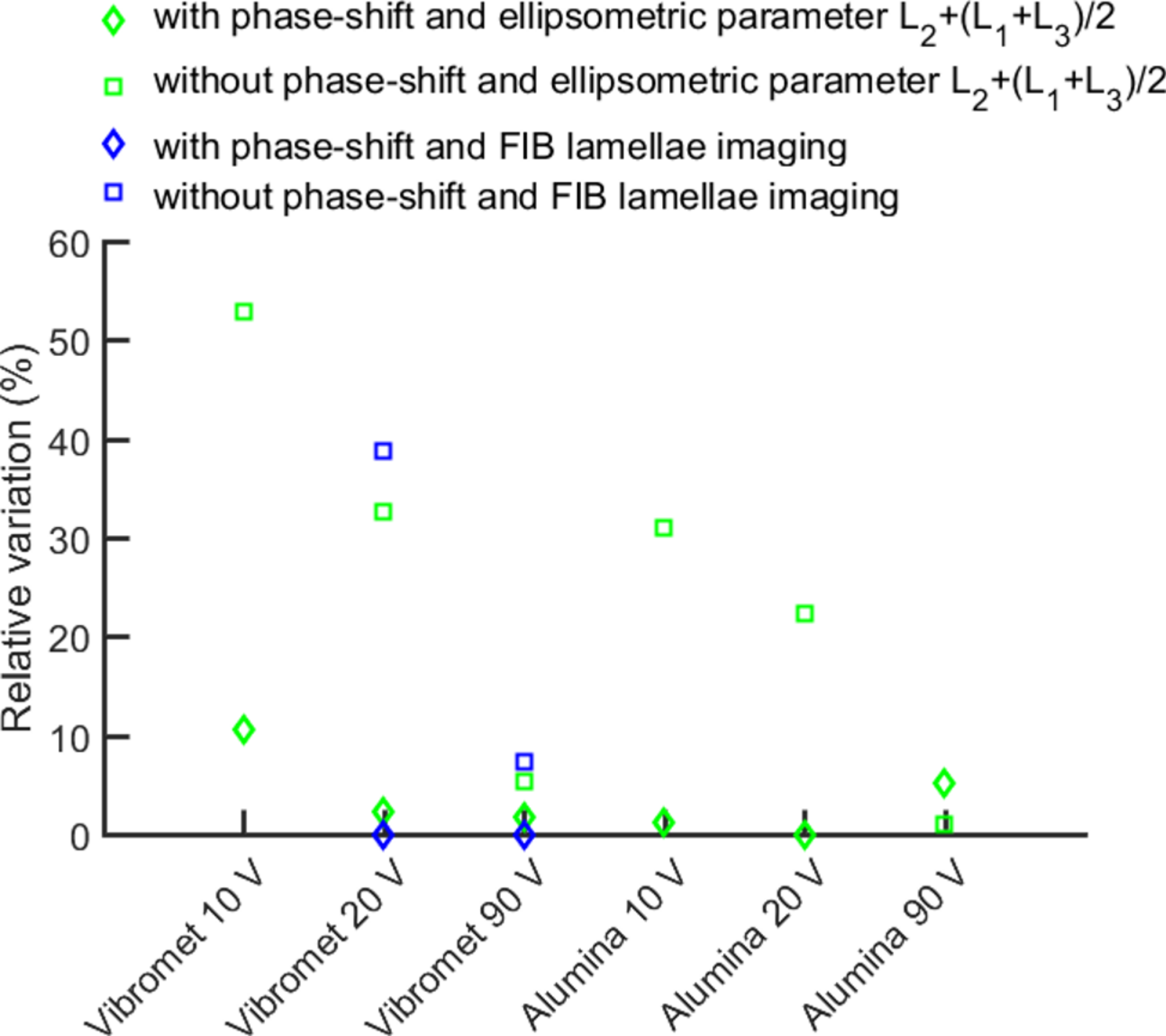
with phase-shift and ellipsometric parameter $L_2+(L_1+L_3)/2$
without phase-shift and ellipsometric parameter $L_2+(L_1+L_3)/2$
with phase-shift and FIB lamellae imaging
without phase-shift and FIB lamellae imaging
Relative variation (%)
60
50
40
30
20
10
0
Vibromet 10 V
Vibromet 20 V
Vibromet 90 V
Alumina 10 V
Alumina 20 V
Alumina 90 V

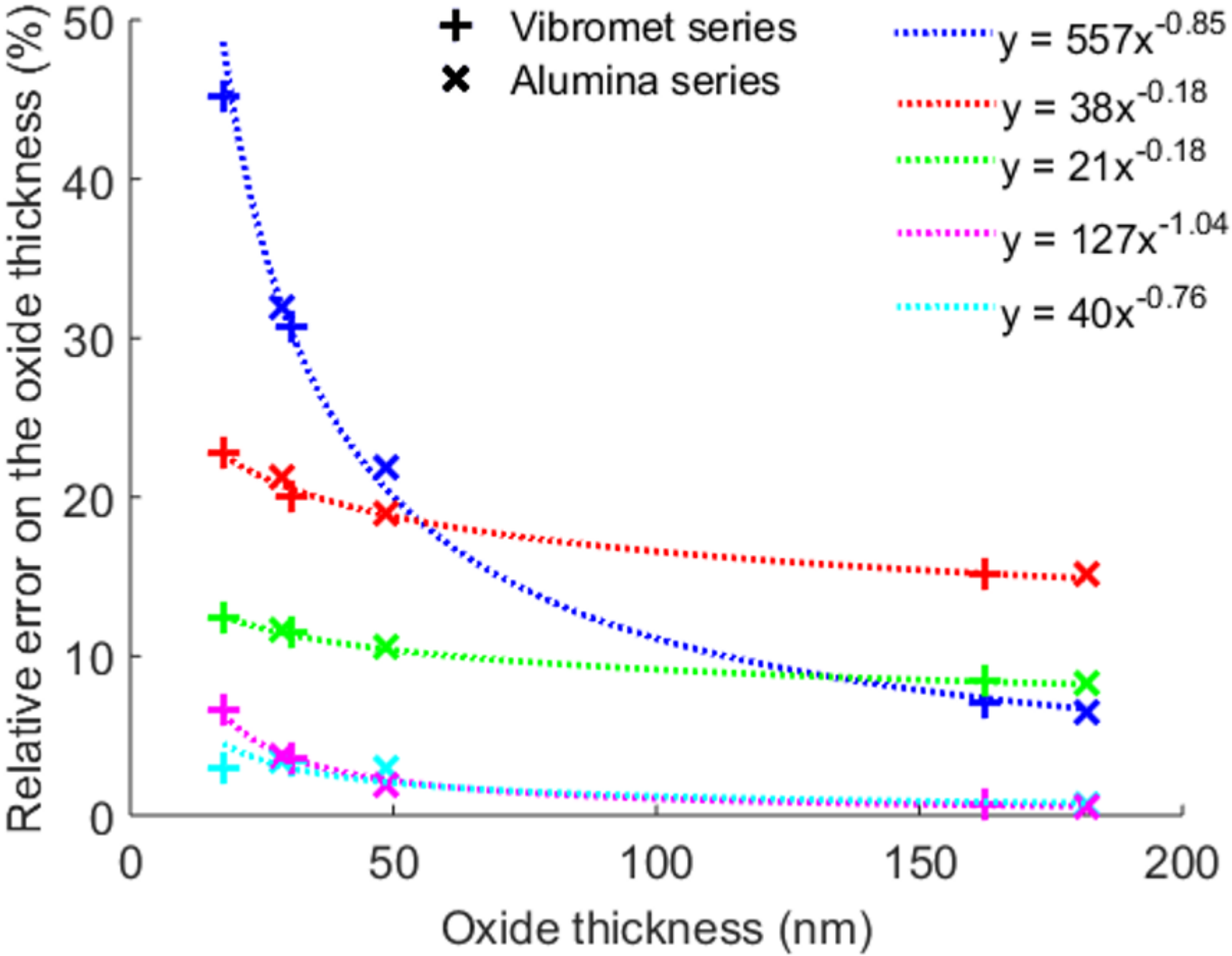
Vibromet series
Alumina series
y = 557x^-0.85
y = 38x^-0.18
y = 21x^-0.18
y = 127x^-1.04
y = 40x^-0.76
Relative error on the oxide thickness (%)
Oxide thickness (nm)
0
10
20
30
40
50
0
50
100
150
200

***X* porosity factor**	**Max. cell potential : 10 V**	**Max. cell potential : 20 V**	**Max. cell potential : 90 V**
Alumina series	0%	0%	13%
Vibromet series	0%	0%	2%

	Vibromet series			Alumina series		
	10 V	**20 V**	**90 V**	**10 V**	**20 V**	**90 V**
L_1 **(nm)**	3	4	31	3	11	39
L_2 **(nm)**	11	27	148	27	41	172
L_3 **(nm)**	6	2	7	2	3	9
$L_1 + L_2 + L_3$ **(nm)**	20	33	186	32	55	220

Oxide layer thickness (nm)	Max. cell voltage: 10 V		Max. cell voltage: 20 V		Max. cell voltage: 90 V	
	phase-shift neglected	with phase-shift	phase-shift neglected	with phase-shift	phase-shift neglected	with phase-shift
Alumina series	46 (2%)	29 (1%)	66 (0.5%)	48 (0.5%)	199 (1.5%)	182 (1.5%)
Vibromet series	34 (0.5%)	18 (2%)	48 (0.5%)	31 (2.5%	180 (1%)	163 (1%)

Reference	Raw material	Electrolyte	Anodizing voltage	Refractive index measurement technique
Joseph et al. [29]	99.9% pure titanium	1 M H_2SO_4	2.5 V to 40 V	ellipsometry
Blondeau et al. [62]	*not indicated*	0.5 M H_2SO_4	[1 V – 48 V] ("amorphous" set) [54 V – 98 V] ("anatase" set)	fit of reflectance spectra
Diamanti et al. [8]	ASTM Grade 2	0.5 M H_2SO_4	60 V ("amorphous" case) 90 V ("anatase" case)	ellipsometry
Van Gils et al. [37]	99.5% pure titanium	0.5 M H_2SO_4	10 V to 80 V	ellipsometry
present work	ASTM Grade 2	0.5 M H_2SO_4	10 V and 20 V ($X = 0\%$) 90 V ($X = 13\%$)	ellipsometry